State-of-the-art passivation strategies of c-Si for photovoltaic applications: A review

Sakti Prasanna Muduli, Paresh Kale [*]

Department of Electrical Engineering, NIT Rourkela, 769008, Odisha, India

ARTICLE INFO

ABSTRACT

The carrier recombination is a major bottleneck in enhancing the power conversion efficiency of first-generation solar cells. As a remedy, passivation minimizes the recombination at the surface and bulk by either neutralizing the dangling bonds or creating a field-effect. The review describes the evolution of the different cell structures based on passivation and classifies the passivation schemes according to the mechanism. The two ways of passivating the crystalline Si are either by reducing the minority carrier concentration at the surface or decreasing the intermediate density of states. Field-effect passivation is achieved by creating an electric field at the surface of Si to repel the minority carriers. The paper compares the typical and emerging dielectric layers in terms of substrate compatibility, effectiveness, interface qualities, and carrier-selective emitters for contact passivation. The effective lifetime of solution-based chemical passivation is compared for various electrolytes. In addition to surface passivation, it describes the advanced hydrogen passivation for bulk defects, such as shielded-hydrogen passivation and laser passivation. Further, the recent developments in the passivation strategies for trending solar cell architectures are discussed from the perspective of challenges.

1. Introduction

The demand for energy produced by solar photovoltaics is increasing due to the scarcity of conventional energy sources. Industries and academics are looking for ways to improve cell efficiency and lower manufacturing cost [1]. First-generation photovoltaic devices, dominated by Silicon (Si) wafer-based technology, show remarkable technical and economic advancements to lower the cost per unit. The single-junction terrestrial Si solar cell achieves the highest efficiency of 26.7% [2,3]. Commercial crystalline Si solar cells with a record efficiency of 22.8% [4], amorphous cells with 10.2% [5] and hetero-junction cells with 22.2% [4,6]; together account for 93% of the current solar cell market [7,8]. Approaches such as improved cell architecture, increasing the number of cell junctions, and using efficient materials [9] are under investigation to increase efficiency [10]. Reducing the semiconductor layer thickness, replacing bulk Si with Si-nanostructures [11], adapting affordable coating processes, and replacing expensive materials with low-cost alternatives are significant ways to lower production costs.

The efficiency of the solar cell is a fraction of the incident power as expressed in equation (1), where V_{oc}, I_{sc}, FF, and P_{in} are the open circuit voltage, short circuit current, fill factor, and incident power, respectively. Thus, FF determines the maximum power of the solar cell in conjunction with I_{sc} and V_{oc} [12,13]. I_{sc} depends on the area of the cell, the spectrum of the incident light, optical properties of the cell surface (absorption and reflection), and minority carrier collection probability. Carrier collection probability is the significant parameter to affect the cell efficiency for a constant area of the cell and the spectrum of the incident light. On the other hand, with an increasing band gap, I_{sc} decreases and V_{oc} increases, leading to band gap optimization for maximum efficiency. Hence, cell architectural modification is the sole remedy for improving the carrier collection probability, light absorption, and band gap optimization.

$$\eta = \frac{V_{oc} I_{sc} FF}{P_{in}} \tag{1}$$

Architectural improvement is one of the practical approaches to enhance cell efficiency. The conventional solar cell structure (Al-back surface field structure) has been used for decades. However, it suffers from low efficiency and high material utilization and is space inefficient [14,15]. The efficiency of Al-back surface field-based (Al-BSF) monocrystalline and polycrystalline Si solar cells is 19.8% and 18.5%,

---

* Corresponding author.
E-mail addresses: pinkusakti08@gmail.com (S.P. Muduli), pareshkale@nitrkl.ac.in (P. Kale).

respectively [16,17]. Passivated Emitter Rear Cell (PERC) structure was first reported in 1980 and was commercially unsuccessful. In recent decades, the PERC (Fig. 1(a)) and modified PERC structures, such as Passivated Emitter Rear Locally-diffused (PERL) and Passivated Emitter Rear Totally-diffused (PERT) (Fig. 1 (b)), together share more than 50% of the solar cell market [18]. The PERL cell possesses diffused layers (heavily doped) at the rear metal contact only, whereas the whole rear surface is diffused in the PERT cell. PERC has reached a commercial efficiency of 21.6% and laboratory efficiency 25% [3,18,19]. The primary reason for shifting from the conventional structure was the increased efficiency due to the introduction of the dielectric layers on the rear surface to minimize the recombination and antireflecting coating (ARC) to reflect heat-generating wavelengths [19,20].

Absence of metal fingers on the front side, the Interdigitated Back Contact (IBC) solar cell (Fig. 1(c)) is an attractive contender for high-efficiency solar cells [21,22] which outperformed PERC with a record efficiency of 26.7% [2,3]. Opening the rear side contact grooves through the dielectric layer in a PERC structure leads to substrate degradation [23]. Tunnel Oxide Passivated Contact (TOPCon) solar cells with a complete area rear side metallic contact (refer to Fig. 1(d)) abstain from difficulties such as the need for laser-aided contact apertures or charge carrier congestion at localized contacts [24,25]. Table 1 lists the passivation-related problems associated with different cell structures and the developments to resolve the issues.

The photo-generated charge carrier recombines on the surface and contact terminals instead of contributing to the current output, reducing the output power and hence the efficiency. The structural evolution of the solar cell figures out the stumbling block to efficiency enhancement-recombination at the surface and the contact region. The review classifies the passivation based on the various recombination reduction techniques. The comparison explains the efficient and effective ways of passivating the c-Si surface (and the bulk) and purpose-based appropriate techniques. Further, it outlines the mechanisms and respective fabrications for each strategy.

1.1. Recombination

In solar cells, charge carrier generation takes place as the result of sunlight absorption. Recombination is the opposite of generation, where the generated carriers within a semiconductor combine with the opposite charge carriers (annihilation). In thermal equilibrium, the generation and recombination rates are identical. The loss of carrier releases energy either as phonons (lattice vibrations) or as photons. Three types of recombination mechanisms are possible in semiconductors, namely, i. Auger recombination, ii. radiative recombination, and iii. Shockley-Read-Hall (SRH) recombination.

When an electron and a hole recombine, the energy is transferred to

Table 1
Advancement of cell structures from the passivation point of view.

Solar cell structure	Passivation related limitations	Resolving development and corresponding cell structure
Al-BSF	A weaker electric field at the rear surface and increased rear surface recombination [26]	Deposition of a suitable dielectric layer and capping layer on the rear (PERC) [27]
PERC	Laser ablation of the dielectric layer for rear contact formation causes defects in the substrate, leading to recombination centers [28]	Full area rear metal contact, tunneling layer separates the substrate and the carrier selective passivation layer (TOPCon) [29]
PERT/ PERL	Front contact through passivation ARC causes defect leading to bulk recombination and optical shading [29]	All rear contact leads to minimizing front surface defect-related recombination loss and optical shading loss (IBC) [30]
IBC	Interdigitated rear contacts by laser ablation increase rear recombination, and consecutive opposite doping narrows the current carrying path [31]	Full area rear metal contact, tunneling layer separates opposite doping layers for carrier selective contact passivation (Tunnel-IBC) [32]

another electron in the conduction band [33], termed Auger recombination. Auger recombination is highly effective in the heavily doped Si-substrates or at high injection levels under concentrated sunlight. During radiative recombination, an electron from the conduction band falls back into the valence band to recombine with the hole. The energy released from the radiative recombination is in the form of a photon having energy equal to the band gap. Radiative recombination is dominant for direct band gap semiconductors [34] and extremely low for indirect band gap c-Si solar cells.

SRH recombination (also known as recombination through defects) takes place through a trap or defect energy level in the band gap [35]. An energy state in the forbidden area traps an electron (or hole), recombining with a hole (or an electron) that climbs to the same energy level. SRH recombination is possible both at the surface and the bulk Si due to dangling bonds and defects, respectively. Surface recombination requires additional attention than bulk recombination due to the high surface-to-volume ratio of a solar cell. Various parameters that indicate the recombination levels are Surface Recombination Velocity (SRV), effective lifetime (τ_{eff}) and the surface saturation current density (J_0). Either SRV or the τ_{eff} describes the degree of passivation for non-diffused n-type or p-type c-Si. However, J_0 explains the same as a function of sheet resistance for excessive dopant-diffused c-Si surfaces.

1.2. Characterization of recombination

The lifetime measurement evaluates the material quality by indicating the possible recombination at the surface and the bulk. Contact-
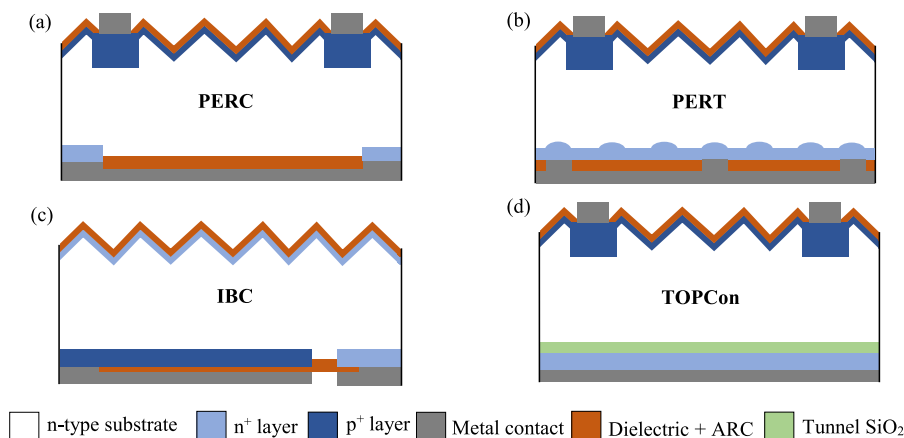
Fig. 1. Structure of n-type (a) PERC, (b) PERT, (c) IBC, and (d) single junction TOPCon cell.

less photoconductance decay or transient measurements are used to determine the τ_{eff} [36,37]. The conductance measurement (photoconductance decay) using the inductive coupling method describes the change in minority carrier concentration [38]. Effective lifetime measurement considers the recombination in bulk and at the surface-termed as bulk lifetime (τ_b) and surface lifetime (τ_s). τ_b includes the contributions of Auger (τ_{Aug}), radiative (τ_{rad}), and SRH (τ_{SRH}) recombination as expressed in equation (2) [39].

$$\frac{1}{\tau_{eff}} = \frac{1}{\tau_b} + \frac{1}{\tau_s} = \left(\frac{1}{\tau_{Aug}} + \frac{1}{\tau_{rad}} + \frac{1}{\tau_{SRH}}\right) + \frac{1}{\tau_s} \tag{2}$$

SRV (S_{eff}) is a derived quantity and is expressed in terms of τ_s as given in equation (3), where W is the substrate thickness, and D is the ambipolar carrier diffusion coefficient [40]. The surface recombination depends on the carriers generated at the bulk and the surface. The carriers generated at the bulk travel to the surface to recombine, whereas the surface-generated carriers recombine instantaneously at the surface or diffuse to the bulk. Hence the SRV is a function of decaying exponential terms (infinite sum) of the surface lifetime, and the dominant first term is expressed in equation (3), which is further simplified with the assumptions-i. same recombination velocity at the front and rear surface, and ii. $(S_{eff}W)/D < 0.25$ [41]. The assumptions put a limitation for the substrate with textured surface, and measurement accuracy decreases to 96% [42]. Further, an assumption of the infinite bulk lifetime results in the maximum S_{eff}.

$$S_{eff} = \sqrt{\frac{D}{\tau_s}} tan\left(\frac{W}{2}\sqrt{\frac{1}{D\tau_s}}\right) \approx \left(\frac{1}{\tau_{eff}} - \frac{1}{\tau_b}\right)\frac{W}{2} \tag{3}$$

The determination of the τ_s requires both τ_b and τ_{eff} and the measurement of the accurate τ_b is a challenging task due to the significant value compared to τ_{eff}. Fig. 2 depicts the effect of changing S_{eff} on τ_{eff} for specified τ_b values [43]. SRV must be reduced below 1 cm s^{-1} to get the effective lifetime below 10% of the for $\tau_b > 2$ ms. The accurate measurement of bulk lifetimes requires excellent surface passivation, particularly in high-efficiency solar cells with $\tau_{eff} > 10$ ms. Similarly, for the τ_{eff} value below 20% of the τ_b SRV should be less than 1 cm s^{-1} for $\tau_b > 3$ ms.

The semiconductor crystal lattice abruptly discontinues at the surfaces, disrupting the band structure and the emergence of a semicontinuum of energy states. The strained and unterminated intermediate states are due to the surface dangling bonds. The well-known SRH

recombination is the most effective way to characterize recombination mediated by band gap states. When estimating the recombination activity of the interface states, a density of interface traps (D_{it}) is approximated at single energy in the middle of the gap ($E_t - E_i = 0$). The electron recombination velocity and the hole capture velocity at the approximated states are $S_{n0} = \nu_{th}D_{it}\sigma_n$ and $S_{p0} = \nu_{th}D_{it}\sigma_p$, respectively [44]. Where ν_{th} and σ are the carrier mean thermal velocity and the capture cross-section of the state, respectively. The effective recombination at the surface is given by equation (4) [45] where Δn_d is the minority carrier concentration at the edge (of width d) of the space charge region. Further, n_s, p_s and n_i are the steady-state electron, hole, and intrinsic electron concentration, respectively.

$$S_{eff} = \frac{U_s}{\Delta n(x=d)} = \frac{1}{\Delta n_d}\frac{n_sp_s - n_i^2}{(n_s + n_i)/S_{p0} + (p_s + n_i)/S_{n0}} \tag{4}$$

The saturation current density (J_0) considers all the recombination mechanisms and heavy doping effects, such as band bending. J_0 characterizes the recombination at the surface for heavily doped emitters and is independent of dopant concentration for undiffused surfaces [46]. Assuming τ_{SRH} to be infinite, J_0 is given by equation (5) [47], where $n_{i,eff}$ is effective intrinsic concentration. Quasi-steady-state photoconductance (QSSPC) or Quasi-steady-state photoluminescence (QSSPL) technique measures J_0 in terms of τ_s [48]. Kimmerle et al. reported a detailed analysis of the J_0 using QSSPC lifetime measurement [49].

$$J_0(\Delta n) = \frac{d}{d\Delta n}\left(n_{i,eff}^2 \cdot \sqrt{D\left(\frac{1}{\tau_s}\right)} tan\left(\frac{W}{2}\sqrt{D\left(\frac{1}{\tau_s}\right)}\right)\right) \tag{5}$$

τ_{eff} varies with the injection level of the substrate; however, the review considers the maximum τ_{eff} (for comparison) which exists in the injection range of 10^{14} to 10^{16} cm^{-3} for non-diffused substrates [49]. J_0 indicates the passivation level for excessive diffused substrates (with an injection level of $\geq 10^{19}$ cm^{-3}). J_0 is expressed in terms of sheet resistance, and the lower the J_0 value, the better the passivation quality. Both τ_{eff} and J_0 characterize the passivation level at the interface of the excessive diffused substrate and the dielectric layer. However, the interface of the excessive diffused substrate and metal contact is characterized by J_0 only.

1.3. Passivation strategies

Various approaches, such as improvement of deposition technique [50,51], utilization of defect-free semiconductor grade wafers [52,53], and passivation, are the primary remedies to reduce the recombination from the surface and the bulk. The recombination is reduced by neutralizing the dangling bonds or restricting the minority carriers. Depending on the recombination mitigation region, the process may be either surface passivation or bulk passivation. State-of-the-art deposition techniques such as atomic layer deposition (ALD) and pure semiconductor grade wafers increase the manufacturing cost in multiple folds [54]. Hence, the economic approach of passivation is preferred to minimize the recombination to increase efficiency and limit the manufacturing cost of the solar cell.

Reducing the minority charge carrier concentration near the surface restricts the recombination, as the maximum possible recombination rate depends on the available minority charge carrier. Minority charge concentration at the surface is reduced by creating an electric field to repel the minority carriers from the surface. Electric field formation at the surface restricts the minority carriers from facilitating recombination at the surface. The two ways of creating the electric field are i. by forming a heavily doped layer and ii. by introducing a dielectric layer.

The carrier deference between the excessive diffused (heavily doped) layer and the normally diffused layer creates the electric field to repel the minority carriers, whereas an external field is applied to charge the dielectric coating-called corona charging. Corona charging enhances
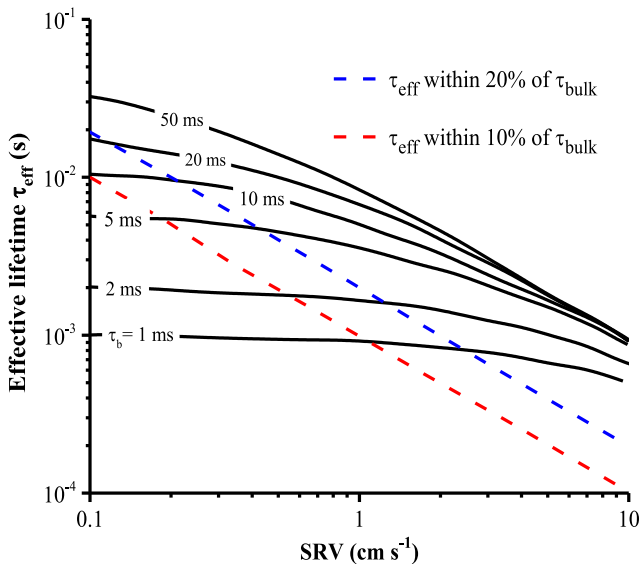

Fig. 2. Impact of varying S_{eff} on τ_{eff} for specified τ_b [43].

field-effect passivation exclusively on a dielectric-coated Si surface, whereas the phrase 'field-effect passivation' encompasses both heavily doped layers and dielectric coatings [55]. Corona charging controls the charge concentration at the interface of c-Si and the dielectric layer to improve the passivation through field-effect passivation [56]. The polarity of the corona charging differs depending on the interface and substrate type. For example, Al_2O_3 is preferable for p-type substrates with negative polarity corona charging, and the SiO_2 dielectric layer passivates a heavily doped n-type emitter with positive polarity charging [57–59]. The other way of passivation is neutralizing the Si surface dangling bonds by hydrogen atoms or oxygen-containing functional groups.

Surfaces (and interfaces in general) create a band of electronic states in the band gap due to broken bonds and impurities, like dislocations and planar defects. The Si surface possesses highly active recombination due to the abundance of band gap states originating from dangling bonds. The strategies for reducing the SRV are mainly of two categories, i. by reducing the carrier concentration at the surface and ii. by reducing the intermediate density of the states (DOS). In practice, both phenomena work together to passivate c-Si on the surface and in bulk. Fig. 3 represents the comprehensive classification of the passivation strategies based on the intrinsic concept and the materials used.

In addition to surface recombination, bulk defects decrease cell efficiency, and conventional passivation techniques complicate the mitigation of bulk defects. The conventional heat treatment for hydrogen passivation through the dielectric layer fails to enhance the effective efficiency of the cell due to the freshly heat-generated defects [60,61]. Shielded hydrogen passivation suggests the formation of atomic hydrogen for passivation without exposing the substrate to excessive temperature (>400 °C) [62,63]. Bulk passivation requires specific techniques, such as LASER-based hydrogen passivation, to eliminate selective bulk defects using different charge states of the atomic hydrogen [64]. In the last decade, several reports explained the chemical passivation in the liquid medium [65–67]; however, applying such chemical passivation in practical fabrication still lacks clarity [43].

2. Field-effect passivation

Field-effect passivation shields the semiconductor interface from minority carriers through an electric field created by either doping profile below the surface or introducing electrical charges in a dielectric layer or a gate electrode [57,68,69]. A heavily doped region forms a high-low junction (such as p^{++}/p) either on the front or rear of the c-Si. The inherent electric field across the junction prevents recombination, thereby repelling the minority carriers towards the bulk part of the c-Si [70,71]. Fig. 4(a) shows a typical both-side-contacted cell structure with the back-surface field (BSF). Electrons and holes from the p-type and n-type c-Si flow away from the respective surfaces towards the bulk due to the intrinsic field formed by the heavily doped regions. The heavily doped layer restricts the minority carriers by increasing the energy level for the valence band of the p-type substrate to the conduction band of the p^+ layer, as shown in Fig. 4(b).

On the other hand, dielectric films combine a chemical reduction of defects states and a sufficient charge concentration for field-effect passivation. Band bending occurs at the c-Si surface, which creates the field to repel the minority carriers towards the bulk portion, thereby preventing them from recombining at the surface [72]. Fig. 4(c) shows the cell structure with front and rear dielectric passivation layers. Depending on the substrate doping type, the field-effect passivation introduces a specific polarity charge into the dielectric layer via corona charging to restrict the recombination at the surface. The band bending concept is the alternative means of representing the dielectric field-effect passivation, as depicted in Fig. 4(d)). The extremely wide band gap of the dielectric layer restricts the recombination on both surfaces [42,72].

2.1. Simulation of field-effect passivation

Solar cell modeling using state-of-art simulation software reduces manufacturing costs. The software packages such as Sentaurus TCAD, EDNA 2, and Quokka 2.2.4 include the Fermi-Dirac model, Schenk's model, and Klaassen's mobility model [73–75]. Schenk's model analyzes the band gap modifications derived from a non-self-consistent finite-temperature full random-phase approximation formalism [75]. Klaassen's first model analyzes carrier mobility, impurity screening, carrier-scattering, impurity-clustering, and the temperature dependence of carrier mobility [73]. Klaassen's second model is especially suitable for complete device simulation, as the carrier mobility is expressed as an analytical function of the carrier concentrations. The model also determines the temperature-dependent carrier lifetime [74]. The SRH model estimates the surface recombination and considers the interface traps distributed across the band gap of the Si [76,77]. The SRH modeling uses equation (4) to estimate the SRV and τ_{eff}. The modeling uses various substrate and dielectric layer parameters, as listed in Table 2. The simulation adapts the QSSPC technique to determine the τ_{eff}. The homogeneous photogeneration of electron-hole pair is considered in a broad wavelength spectrum to study the injection dependent τ_{eff}.
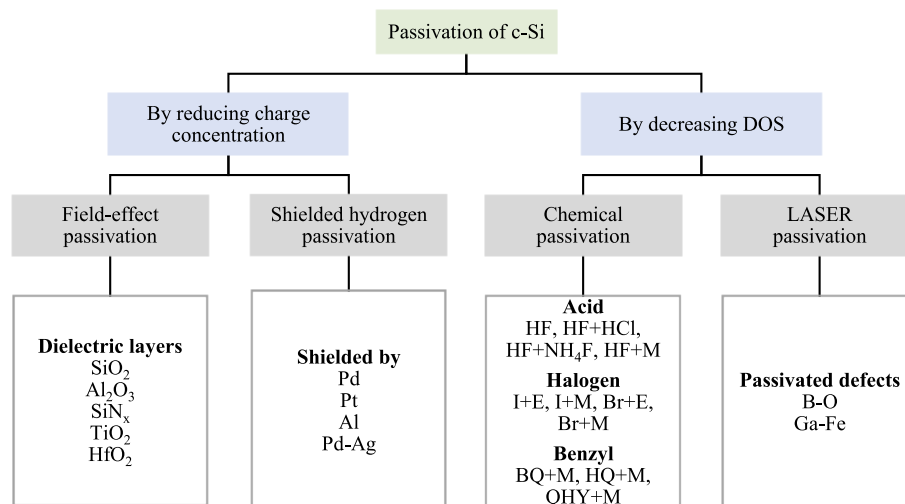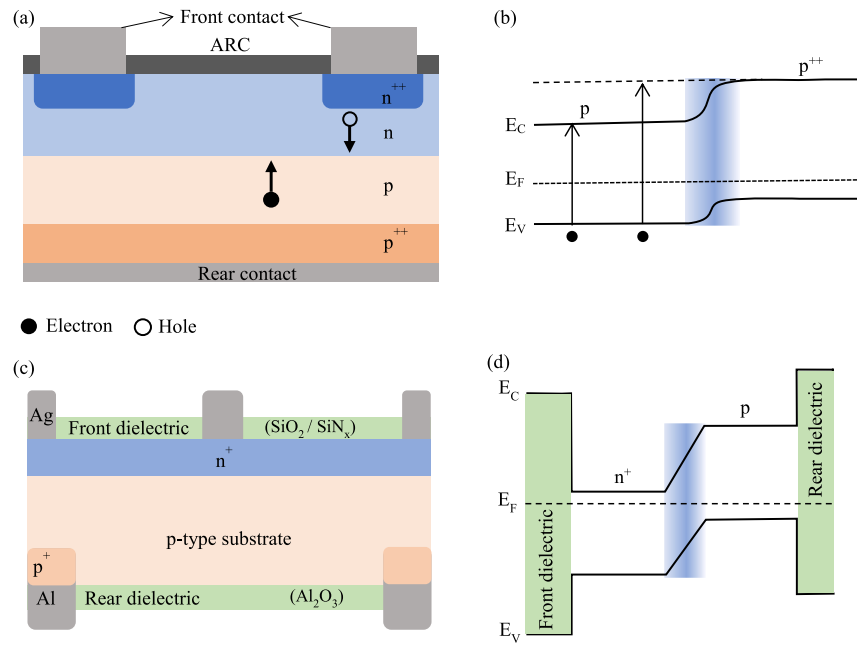

Fig. 3. Classification of passivation strategies; where M − Methanol, E− Ethanol, I- Iodine, Br- Bromine, BQ-*p*-Benzoquinone, HQ- Hydroquinone, QHY- Quinhydrone, B–O- (Boron–Oxygen) defect, Ga-Fe- (Gallium–Iron) defect.

Fig. 4. (a) Generalized concept of field-effect passivation by increasing doping level, (b) band structure of doping level increment, (c) cell structure showing dielectric layers, (d) band structure of dielectric passivation.

Table 2
Typical values of the parameters used in the simulation extracted from experimental studies.

	Parameters		Typical reported value	Ref.
Substrate parameters	Thickness (μm)		100–300	[42]
	Resistivity (Ω.cm)		1–5	
	Doping level for undiffused substrate (cm^{-3})		$(1-5) \times 10^{15}$	[78,79]
	Doping level for heavily diffused substrate (cm^{-3})		$(1-6) \times 10^{19}$	
	Surface crystalline structure		{100}	[80]
Dielectric layer parameters	Electron/hole capture density (cm^{-2})		10^{16}	
	Fixed charge density at the interface (cm^{-2})	Al$_2$O$_3$	$-(10^{12} - 10^{13})$	[76,79,81]
		SiO$_2$	2×10^{11}	[82]
		SiN$_x$	3.6×10^{12}	[83]
		TiO$_2$	-4.9×10^{12}	[84]
		HfO$_2$	1.64×10^{12}	[85]

Dumbrell et al. reported that the effect of single-side metalization of the substrate decreases the lifetime due to excessive recombination at the contact area [48]. The lifetime decreases from 2 ms to 0.5 ms due to the elimination of the dielectric layer from one side of the p-type substrate, followed by Al deposition (500 nm). Ma et al. investigated the effect of polarity inversion of the corona charging of the Al$_2$O$_3$ layer on the n-type and p-type substrate [80]. Maximum τ_{eff} drops from 1.7 ms to 0.45 ms for n-type and 1.8 ms–0.3 ms for p-type substrate while reversing the polarity from negative to positive for a 15 nm Al$_2$O$_3$ layer. The inversion of the corona charging polarity modifies the fixed charge density in the dielectric layer and generates additional interface traps at the surface of c-Si (surface damage), leading to a decrement in the lifetime. Table 3 presents the insight of simulated passivation of c-Si with various dielectric layers.

Anand et al. [25] optimized the TOPCon cell performance by varying

the tunnel oxide (SiO$_2$) thickness (ranging from 0 to 1.1 nm) and BSF doping level (ranging from 10^{15} cm^{-3} to 10^{21} cm^{-3}) using the numerical tool AFORS-HET. The tunneling efficiency decreases with increasing oxide thickness and rises with increasing doping concentration. The increase in oxide thickness improves the passivation, lowers the contact resistivity, and allows selective passage of the charge carrier via tunneling. The high BSF doping lowers the recombination current and improves the overall cell performance. With optimized BSF doping level (= 10^{19} cm^{-3}) and tunneling oxide layer thickness (= 1 nm), V_{oc} increases by 5.5%, I_{sc} increases by ~13%, and 25% efficiency improvement is observed.

2.2. Dielectric layers deposition techniques for field-effect passivation

The dielectric layer deposition depends on substrate doping type,

Table 3
Simulated lifetime measurement of field-effect passivation.

Substrate doping type and Resistivity (Ω.cm)	Substrate thickness (μm)	Dielectric layer	Dielectric layer thickness (nm)	Maximum τ_{eff} (ms)	Mathematical tool	Ref.
p, 2	275	Al$_2$O$_3$	15	2	Sentaurus TCAD	[80]
n, 1.9	300			2.5		
n, 5	710	Al$_2$O$_3$/SiN$_x$	–	2	Quokka	[48]

post-deposition processes, and substrate roughness (plane or textured). The substrate doping type and level decide the dielectric material as a specific dielectric layer is compatible with a particular substrate type. The post-deposition processes include Al etching, laser ablation for contact formation, heavily diffused Si layer deposition, and antireflecting layer coating (ARC).

The dielectric layer deposition on a plane Si substrate is compatible with all possible deposition techniques, whereas a textured surface needs sophisticated deposition techniques such as ALD and Plasma Enhanced Chemical Vapor Deposition (PECVD) (because of effectiveness and material purity). The textured front surface enhances the photon trapping capability; however, the recombination increases due to the high surface area (an upright pyramidal structure is a commonly reported texture with an area ~1.73 times the flat surface) [86]. The texturing converts the surface orientation to {111} compared to a flat surface with {100} orientation, creating excess dangling bonds and interface defects [87]. Instead of the double-side polished substrate, the textured surface results in high I_{sc} due to low reflection; however, the V_{oc} decreases because of higher recombination [67]. Hence the passivation of a textured surface is a challenging task to achieve the τ_{eff} comparable to a flat surface.

Deligiannis et al. [67] studied the τ_{eff} of textured c-Si with three consecutive nitric acid oxidation cycles (NAOC) after standard cleaning and PECVD-grown intrinsic hydrogenated amorphous Si. The NAOC enhances the τ_{eff} of the textured surface equivalent to that of a flat surface. With surface texturing and field-effect passivation (SiO₂), the efficiency of the Si solar cell increases from 9.8% to 15.04%, as reported by Qiu et al. [88]. Table 4 lists the passivation of the rear and front surface with different dielectric layers with the highest reported τ_{eff}.

One of the simple and cost-effective ways of back surface passivation is the screen printing of Al, followed by annealing at high temperatures to form a p^+ layer called an aluminum back surface field (Al-BSF). However, Al-BSF is possible only for p-type substrates, and the field (formed because of the p^+ layer) is weaker than the field developed across the dielectric layer after corona charging. Hence, high-efficiency PERC uses dielectric surface passivation and local contact formation, unlike the conventional Al-BSF [42]. Various dielectric layers, mainly thermally grown SiO₂ [95], Si nitride (SiN$_x$) by PECVD [92], and an atomic layer deposited TiO₂ [93] lead to SRV of less than 200 cm s^{-1} at the injection level of 10^{14}-10^{15} cm^{-3}. The commonly reported dielectric materials for the surface passivation of c-Si are SiO$_x$, SiN$_x$, Al₂O₃, TiO₂, and the stacking of multiple dielectrics.

SiO$_x$: The conventional way of oxide layer formation is thermal oxidation performed in an oxygen environment (temperature >1000 °C for at least 30 min), followed by cooling under an argon atmosphere

[95]. The passivation obtained by the oxide layer formation is further improved by forming gas (95% N₂, 5% H₂) annealing (425 °C under forming gas for 25 min).

The *alneal* is improved annealing, whose main objective is to passivate the dangling bonds of the surface by the atomic hydrogen. During alneal, the sample is annealed (at 400–450 °C in the forming-gas atmosphere) after a thermally evaporating aluminum layer (0.1 μm–1 μm thick) on thermally grown SiO₂ [97]. Finally, the Al layer is etched using hot phosphoric acid (80 °C) [97]. The reaction between the Al and the hydroxyl ions (or water molecules in the SiO₂ layer) produces atomic hydrogen [98] that diffuses through the SiO₂ layer and passivates the dangling bonds [99]. Hydroxyl ions are the prominent source of atomic hydrogen, as heating at 100 °C removes the water molecules, whereas hydroxyl ions require vacuum heating at 600 °C [100]. The presence of the Al on the oxide surface creates an electric field that causes injection of the atomic hydrogen into the oxide and improves the drift towards the Si–SiO₂ interface [101]. The driving field is due to the lower work function of the Al (4.2 eV) [102] compared to SiO₂ (5.05 eV) [103,104]. The importance of the Al coating was verified by Collett et al. [101] by coating Au (with a work function of 5.1 eV) and proved the inability of Au to introduce the ions into the oxide layer. The enhanced alneal reduces the overall processing time and charge introduction during the Al deposition, and hydrogenation takes place simultaneously [101]. Instead of only phosphoric acid, enhanced alneal uses a mixture of phosphoric acid (60%), acetic acid (3.5%), and nitric acid (2.5%).

SiN$_x$: High effective lifetime of ~4.3 ms is possible by forming SiN$_y$/SiN$_x$ double layers on the rear side of the p-type Si [92]. Firstly, SiN$_y$ passivating layer and, after a wet chemical RCA process, SiN$_x$ capping layer is deposited by direct plasma and remote plasma PECVD, respectively. In both processes, NH₃ content is varied in the SiH₄ + NH₃ + H₂ gas mixture to control the refractive index of passivating and capping layers. Nguyen et al. used HF-methanol solution to wash the wafer prior SiN$_x$ deposition by catalytic chemical vapor deposition (cat-CVD) to improve the passivation by increasing the wettability of the fine-textured n-type c-Si and reported the τ_{eff} of ~7.8 ms with SRV of ~0.6 cm s^{-1} [91].

The thermally grown SiO₂ layer was the commonly adapted technique for passivation in 1980–90 because of the ease of the deposition [105,106]. Low-temperature PECVD-coated SiN$_x$ is used as one of the alternatives to thermal oxidation to avoid the high-temperature process. SiN$_x$ outperforms the passivation properties of SiO₂ and is also suitable for both normally doped and heavily doped c-Si [107–111]. The factors that popularize the PECVD-grown SiN$_x$ are its antireflecting property and the excellent passivating property (comparable to thermally grown SiO₂) even after high-temperature firing. The 'alneal' and 'enhanced alneal' were parallel development to the SiN$_x$, which again proved the

Table 4
Summary of significant field-effect passivation materials.

Surface fields	Dielectric material	Substrate doping type, Resistivity (Ω.cm)	Wafer thickness (μm)	Fabrication process	Maximum τ_{eff} (ms)	SRV (cm. s^{-1})	Ref.
BSF	Al₂O₃	p, 1-4	190	ALD	0.01	–	[89]
				ALD + front and rear SiN$_x$	0.175	–	
				ALD + front and rear SiN$_x$ + firing	0.895	–	
				ALD + front and rear SiN$_x$ + firing + Al removal	0.765	–	
	SiO$_x$/SiN$_x$ SiO$_x$/SiN$_x$/ SiO$_x$N$_y$	p, 1	250	PECVD + annealing	0.15 0.2	~70 ~60	[90]
	SiN$_x$	n, 1-5	280	Catalytic-CVD	7.8	0.6	[91]
	SiN$_y$/SiN$_x$	p, 2-3	290	PECVD	4.53[a]	3.2	[92]
FSF	TiO₂	p, 10	140	ALD	~0.85	~14	[93]
		p, 1			~0.2	~54	
		n, 1000	500		~0.9	–	[94]
	SiO₂	p, 1.25	–	Thermal oxidation	–	~10	[95]
		–			–	~24	
		n, 1	265		4	~2.6	[96]

[a] Calculated considering infinite bulk lifetime.

effectiveness of the thermally grown SiO_2 [101].

$SiO_x/SiN_x/SiO_xN_y$: SiO_xN_y capping layer improves the defect passivation and prevents the interaction between the Al contact and SiO_x/SiN_x passivation on the rear side [90]. PECVD-coated SiO_xN_y layer improves the passivation by 30% compared to SiO_x/SiN_x passivation. The thickness of the layer must be more than 200 nm for better protection of the SiO_x/SiN_x stacking layer.

Bonilla et al. simulated the $Si–SiO_2$ interfaces using the TCAD software package for PERC cells and reported a 1% improvement in power conversion efficiency [112]. The interface trap density of the $Si–SiO_2$ and $Si-SiN_x$ are 4×10^{11} eV^{-1} cm^{-2} and 10^{11} eV^{-1} cm^{-2}, respectively [113,114]. Forming gas annealing of SiO_2 and SiO_x/SiN_x improves the passivation quality by reducing the interface trap density to 5×10^{10} eV^{-1} cm^{-2} and 10^{10} eV^{-1} cm^{-2}, respectively [112].

Al_2O_3: Huang et al. [89] reported ALD of Al_2O_3 (~10 nm) on the rear surface of the p-type c-Si at 200 °C in an O_3 environment after HCl and HF cleaning. Then SiN_x layer (100 nm) is deposited on both the front and rear surface by PECVD and fired at ~760 °C. SiN_x layer acts as the ARC and capping layer on the front and rear surfaces, respectively. The dielectric layer (commonly SiN_x) covers the major area of the front surface for effective passivation as well as ARC. The metalization typically covers 2–5% of the area to minimize the shadowing and recombination losses. However, in the case of the Al electrode, the cost-effective screen-printed Al electrode covers up to 20% of the rear side, and the Al_2O_3/SiN_x stack covers the rest area. Dingemans et al. investigated the interface quality of the $Si–Al_2O_3$ interface and reported the minimum interface trap density of 0.4×10^{11} eV^{-1} cm^{-2} for Al_2O_3 deposited by water-based ALD followed by annealing at 350 °C (SRV of 4 cm s^{-1}), whereas maximum fixed charge density of 5.6×10^{12} cm^{-2} for plasma-based ALD followed by annealing at 450 °C (SRV of 2.8 cm s^{-1}) [115].

SiO_2/Al_2O_3: Among the stacking of multiple dielectric layers for the passivation, SiO_2/Al_2O_3 is extensively reported after SiO_2/SiN_x stacking. The SiO_2 layer is grown by thermal oxidation, whereas either ALD or PECVD deposits the Al_2O_3. The significant investigation on the stacking of SiO_2/Al_2O_3 started after the report of additional ultrathin SiO_2 layer formation on the c-Si surface during Al_2O_3 by Stesmans et al. [116]. The forming gas annealing after the thermally grown SiO_2 introduces hydrogen ions, and rapid thermal annealing (30 °C.min^{-1}) of SiO_2/Al_2O_3 in the N_2 atmosphere passivates the Si surface [99]. Dingemans et al. showed the dependency of passivation properties on the annealing temperature, annealing duration, and the mass density of the Al_2O_3 layer for ~190 nm thermally grown SiO_2 and ~100 nm ALD-deposited Al_2O_3 [99]. Hydrogen diffusion in molecular from is possible in low-density Al_2O_3 films (2.9 g cm^{-3}) annealed at a temperature over 600 °C and in atomic form for a dense film (3.2 g cm^{-3}) annealed at a temperature between 300 °C and 600 °C. The effective SRV is drastically reduced by 60% for SiO_2/Al_2O_3 stacking from SiO_2 monolayer [117].

TiO_2: Gad et al. [93] reported the deposition of TiO_2 on the front surface of p-type c-Si by ALD at 150 °C and 200 °C by using tetrakis (dimethyl amido) titanium ($C_8H_{24}N_4Ti$) as Ti precursor and water vapor as oxidant (plasma enhanced ALD). The alternative source of Ti for ALD is titanium isopropoxide and titanium tetrachloride (heat-assisted ALD), along with DI water as the source of oxygen [94,118].

The passivation mechanism at the $Si–TiO_2$ interface differs from other dielectric layers as the forming gas annealing cannot introduce atomic hydrogen into the ALD-deposited TiO_2 layer due to the insufficient activation energy (0.37 eV) for hydrogen diffusion [119]. Further, Miyagawa et al. proved the same for post-ALD hydrogen plasma treatment [120]. The plausible passivation mechanism is forming Si–O–Ti bonds by dissociating the Si–H and Si–H_2 bonds [119,121].

HfO_2: As a passivation layer for n-type c-Si, hafnium oxide (HfO_2) is preferable due to its positive fixed charges and thermal stability [122]. ALD preferably deposits HfO2ither as a monolayer or along with a SiN_x:H capping layer [123]. The interface trap density of ALD-deposited HfO_2

can be reduced to the order of 10^{12} eV^{-1} cm^{-2} and controlled to positive and negative fixed charge by deposition conditions and post-deposition treatments [123]. Zhang et al. [122] reported the deposition of the HfO_2 by remote plasma ALD and simulation of PERC for rear surface HfO_2/-SiN_x:H passivation and capping layer. The τ_{eff} increases from 0.015 ms to 0.074 ms with post-deposition annealing temperature from 400 °C to 500 °C and a further increase in temperature (650 °C) reduces the τ_{eff} to 0.019 ms. The interface quality investigation proved the reason for τ_{eff} variation trend. The interface trap density reduces from 50×10^{12} eV^{-1} cm^{-2} to 5×10^{12} eV^{-1} cm^{-2} for annealing temperature of 500 °C (as a result τ_{eff} improves), and further elevation of temperature increases the defect density (as a result τ_{eff} degrades). The other plausible cause for the τ_{eff} degradation is the rapid decrease in fixed charge density above 500 °C of post-deposition annealing temperature.

Although ALD and PECVD are effective and commonly used techniques for dielectric layer deposition, both ALD (plasma-assisted) and PECVD cause bulk defects in c-Si due to high-energy charged particles and UV rays in the plasma. The shielded hydrogen passivation (SHP) is an extended version of field-effect passivation to mitigate the harmful effect of plasma and introduce atomic hydrogen (using PECVD) to the bulk for defect passivation.

2.3. Field-effect passivation at different interfaces

The schematic of a typical commercial bifacial structure is given in Fig. 5 to explain the passivation at the four different interfaces [72] for field-effect passivation at interface I. excess dopant-diffused c-Si, II. non-diffused c-Si, III. the interface of metal contact and the electron selective region, and IV. the interface of metal contact and hole selective region.

2.3.1. Interface I: excess dopant-diffused c-Si
Thermally grown SiO_2 effectively passivates the n^+; however, owing to several design constraints, including the high manufacturing cost and the sensitivity of the silicon bulk material to high temperatures, high-temperature oxidation is not ideal for industrial solar cells [72]. The alternative low-temperature passivation scheme, chemical-vapor-deposited SiN_x, outperforms SiO_2 passivation and is preferable for industrial solar cells due to the tunable refractive index and ease of screen-printed contact formation [124]. As shown in Fig. 6(a), alnealed-SiO_2 further decreases the J_0 (compared to SiN_x passivation) due to atomic hydrogen introduction [101].

However, to avoid the Al deposition and chemical cleaning involved in the alneal, the SiO_2 and SiN_x layer stacking provides the same effective passivation as the alnealed SiO_2 [125]. Considering the simplicity of
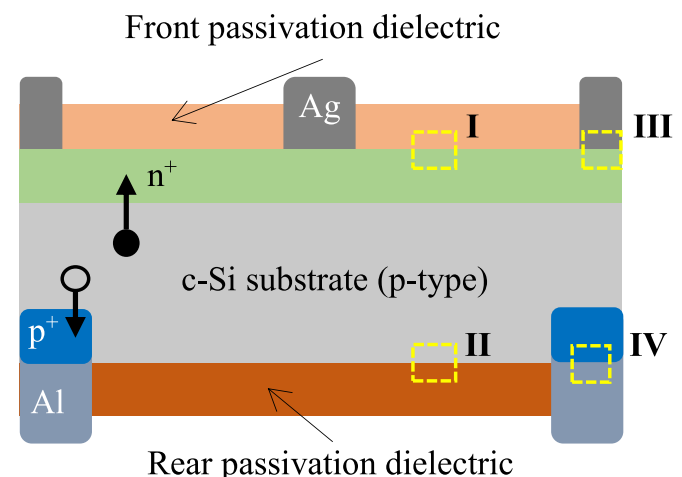

Fig. 5. Standard cell structure with possible interfaces for passivation.
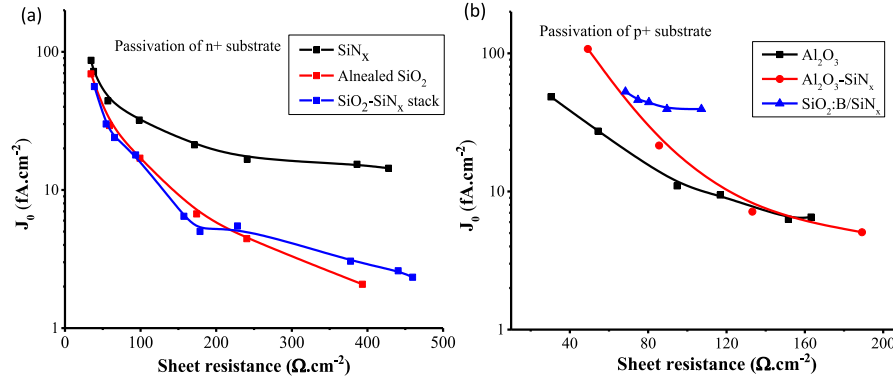
Fig. 6. Comparison of saturation current density of passivation with various materials for (a) n$^+$ substrate [125], (b) p$^+$ substrate [126–128].

SiO$_2$ deposition and the antireflecting property of SiN$_x$, stacking of the SiO$_2$ and SiN$_x$ (SiO$_2$/SiN$_x$) is the preferable passivating method for the n$^+$ emitter. The high hydrogen concentration in the PECVD-SiN$_x$ layer contributes to the improved passivation performance of the SiO$_2$/SiN$_x$ stack. Fig. 6(a) shows the saturation current density of the n$^+$ substrate passivated by different dielectric layers.

For boron-diffused p$^+$ emitter, passivation through thermally grown SiO$_2$ is unstable and causes degradation in the voltage output. The instability is due to the permeability of the SiO$_2$ layer, which forms a moisture barrier and restricts passivation [129–131]. SiN$_x$ is detrimental for p$^+$ emitter due to the high positive fixed charge density and asymmetric electron-hole capture cross-section ratio of the interface states [132]. The passivation level for the p$^+$ substrate is lower than that of the n$^+$ emitter with either SiO$_2$ or SiN$_x$ layer.

However, due to high negative fixed charge density, Al$_2$O$_3$ deposition on the p$^+$ layer results in excellent passivation [126] and stability (even under prolonged UV radiation) performance [113]. Richter et al. reported that the Al$_2$O$_3$/SiN$_x$ stacking layer passivation outperforms pure Al$_2$O$_3$-based passivation for substrates with sheet resistance greater than 130 Ω cm^2 [127]. The modified PERC cell structure uses PECVD grown boron silicate glass (BSG) layer instead of the Al$_2$O$_3$/SiN$_x$ stack (PERT). Though the BSG results in inferior passivation quality compared to Al$_2$O$_3$/SiN$_x$ stacking (Fig. 6(b)), it acts as the source of boron for the p$^+$ emitter and a passivation layer, thus making it favorable for industrial cell fabrication.

2.3.2. Interface II: passivation of normally-doped c-Si

The passivation of the rear p-type substrate is one of the technological advancements to achieve higher efficiency. As explained earlier, SiN$_x$ passivation replaces the high-temperature thermal deposition of SiO$_2$. The high density of the fixed positive charge of the SiN$_x$ creates an inversion layer on the c-Si, and the connection of the inversion layer to the base contact causes a considerable reduction in short-circuit current density (known as 'parasitic shunting') [133]. Annealing of the SiN$_x$ passivated c-Si reduces τ_{eff} for annealing duration longer than 200 min, unlike SiO$_2$ passivation (τ_{eff} saturates for prolonged annealing) [125]. Schmidt et al. prove that an intermediate thermally grown SiO$_2$ layer between p-type c-Si and SiN$_x$ prevents parasitic shunting [125]. The hydrogen diffusion occurs from PECVD-grown SiN$_x$ to the c-Si and oxide interface to neutralize the dangling bonds, which improves the passivation of the SiO$_2$/SiN$_x$ stack.

Al$_2$O$_3$ removes the parasitic shunting due to the fixed negative charges [134,135]; however, the firing (~800 °C) of industrial solar cells after applying the screen-printed metal paste (Al) degrades the passivation layer (ultrathin Al$_2$O$_3$). The SiN$_x$ capping layer improves the stability [136], protecting the Al$_2$O$_3$ layer from Al contact [137]. From Fig. 7, Al$_2$O$_3$/SiN$_x$ results in τ_{eff} of almost two times that of SiO$_2$/SiN$_x$ for the p-type substrate.
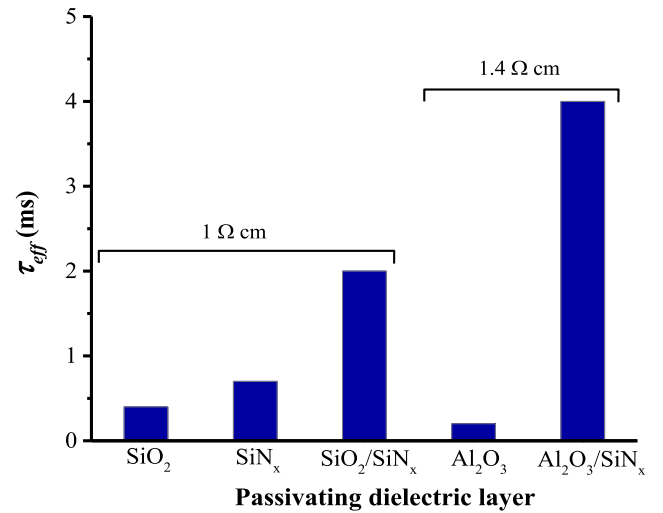

Fig. 7. comparison of τ_{eff} of passivation of p-type substrate [125,137].

Table 5
Effectiveness of the dielectric layer with the substrate (based on τ_{eff}).

Dielectric layer	Doping type			
	p	n	p$^+$	n$^+$
SiO$_x$	✓	✓	✕	✓✓
SiN$_x$	✓	✓✓	✕	✓
Al$_2$O$_3$	✓✓	✕	✓✓	✕
TiO$_2$	✓✓	✓	✓	✓
HfO$_2$	✓	✓✓✓	✓	✓✓
SiO$_2$/SiN$_x$	✓✓	✓✓✓	✓	✓✓✓
SiO$_2$/SiN$_x$/SiO$_x$N$_y$	✓✓	✓✓	✓	✕
Al$_2$O$_3$/SiN$_x$	✓✓✓	✓	✓✓✓	✓
SiO$_2$/Al$_2$O$_3$/SiN$_x$	✓	✓	✓✓✓	✓✓

✕ - ineffective, ✓ - less effective, ✓✓ - moderately effective, ✓✓✓ - highly effective.

Though a single dielectric layer passivates the c-Si surface, the SiN$_x$ layer further improves the lifetime both for the SiO$_2$ with a positive fixed charge and Al$_2$O$_3$ with a negative fixed charge. SiN$_x$ layer acts as the positive charge introducer ARC [124] for SiO$_2$ and the protective capping layer for Al$_2$O$_3$ [136]. The typical PERC structure (p-type substrate) with the n$^+$ emitter on the front and either p or p$^+$ on the rear surface requires SiO$_2$/SiN$_x$ and Al$_2$O$_3$/SiN$_x$ as the front and rear passivation layer [138]. The detailed analysis in Table 5 summarizes the compatibility and effectiveness of the dielectric layers with the substrate

type.

2.3.3. Interface III and IV: Carrier selective contact passivation

The metal-semiconductor interface suffers from strong recombination, restricting the enlargement of the metal contact area on the cell structure. A highly doped n^+ (or p^+) region underneath the metal contact allows electrons (or holes) from the c-Si reducing recombination velocity [139]. An electron-selective n^+ emitter at the negative-metal contact permits electrons to flow from the c-Si wafer to the contact. The poor hole conductivity of the n^+ emitter prevents holes from reaching the recombination sites reducing the saturation current density. As shown in Fig. 5, the photo-generated electron flows towards the screen-printed Ag electrode (front surface) through the electron-selective P-diffused n^+ emitter. The hole travels to the screen-printed Al contact (rear surface) through Al-doped hole-selective p^+ region. Increasing the doping level beneath the metal contact further enhances the passivation of the emitter (selective emitter) [140]. A hole-selective zone isolates the positive contact from the c-Si wafer and is locally produced by Al-doped back surface field during the firing. Holes can readily flow through the hole-selective zone inhibiting electrons and resulting in a low recombination current density [141]. Table 6 lists the reported carrier-selective layers for contact passivation with respective saturation current density (J_0) and contact resistance (ρ_c).

3. Shielded hydrogen passivation (SHP)

The defect elimination uses hydrogen incorporation into Si to achieve excellent passivation of surface and bulk defects [153,154]. Some of the Si PV structures, especially screen-printed cells, require high-temperature firing to release the hydrogen in dielectrics (such as SiN_x [155] and Al_2O_3 [156]). The architectures based on Si heterostructures need hydrogen introduction at low temperatures to avoid heat-generated defects at the interfaces [157]. SHP introduces sufficient atomic hydrogen at low temperatures using modified PECVD with ammonia as the H source [158]. During SHP, a metallic shield, either of palladium (Pd) or Pd-alloys [159], electrically connected to the ground

Table 6
Carrier selective emitter for passivation of metal-semiconductor interface.

Type	Passivation layer	Deposition technique	J_0 (fA. cm^{-2})	ρ_c (Ω. cm^2)	Ref.
Electron-selective contact passivation	MgO$_x$	Sputtering	~950	0.018	[142]
	P-diffused n$^+$	Screen-printing	109	0.26	[143]
	SiO$_x$/TiO$_2$	TO/ALD	50	0.026	[144]
	SiO$_x$/poly-Si (n$^+$)	TO/LPCVD	5	0.016	[145]
			2.7	0.0013	[146]
			30	0.001	[147]
	SiO$_x$/SiN$_x$/ poly-Si (n$^+$)	TO/PECVD/ PECVD	3.7	0.1	
	a-Si:H(i)/a-Si:H (n)	PECVD	2	0.1	[148]
	MoO$_x$ on n	TE	~300	0.03	[149]
Hole-selective contact passivation	Al-doped p$^+$	Screen-printing	~550	0.005	[150]
	MoO$_x$ on p+	TE	~200	0.0002	[149]
	MoO$_x$ on p		~200	0.001	
	SiO$_x$/poly-Si (p$^+$)	TO/PECVD	~35	0.01	
			16	0.008	[147]
	SiO$_x$/Si:C (p$^+$)	CO/PECVD	~12	0.017	[151]
	a-Si:H(i)/ MoO$_x$	PECVD/TE	10	0.4	[152]
	a-Si:H (i)/a-Si:H (p)	PECVD	2	0.4	[148]

a-Si – amorphous silicon, a-Si:H (i) – hydrogenated intrinsic amorphous silicon, poly-Si – polycrystalline silicon, TO – thermal oxidation, TE – thermal evaporation, CO – chemical oxidation.

to neutralize the energetic ions striking the sample [158], protects the wafer from the harmful effects of the hard UV photons [62]. Fig. 8(a) shows the schematic of the arrangement for the metal shield in the plasma chamber. An aluminum grid holds the shield, and the shield thickness depends on the chamber temperature and pressure.

According to Pick et al. [160], the Pd shield absorbs the atomic hydrogen after the dissociation of the H_2. The hydrogen atom diffuses through the shield and combines with a nearby H atom to form H_2 on the opposite surface (Fig. 8(b)). Though the theory is well-referred, it fails to explain the formation of atomic hydrogen after diffusion through Pd. The Si surface receives the atomic hydrogen and gets passivated, so there may be different phenomena behind the dissociation of the H_2 on Pd [159,161,162]. Lisowski et al. suggest the plasma source forms the hydrogenated palladium (Pd–H) film and post-high-temperature treatment decomposes to release atomic hydrogen [163]. Tyurin et al. raise the energy level of the H on the Pd surface by ion bombardment, and the diffused excited atomic hydrogen through Pd exhibits delays in further combination to form H_2 [164].

The Pd shield should be oxide-free and sulfur-poisoned (HS-treated Pd) to improve the atomic hydrogen diffusion and molecular dissociation on the surface [165]. Palladium oxide (PdO) restricts the atomic hydrogen diffusion, and the hydrogen plasma treatment in PECVD removes the oxide layer from the Pd surface. Sulfur increases the probability of sticking and the dissociation of the H_2 on the Pd surface. Although numerous hypotheses explain atomic hydrogen passivation, one plausible explanation is that Si–H bonds form at a quicker rate than H_2 formation from H atoms. In addition to Pd, other metal shields such as Pt, Al, and Ni [39–42] cause hydrogen dissociation; however, no report claims any of these metals can introduce atomic hydrogen for passivation below 400 °C and as diffusive as Pd.

Bourret-Sicotte et al. performed SHP on 200 μm thick, 1 Ω cm, n-type float zone Si samples with a 100 nm thermally grown SiO$_2$ for 45 min at 380 °C using sulfur-poisoned Pd shield and reported the lifetime of the passivation enhanced from 12 to 1050 μs [159]. Corona charging further enhanced the lifetime to 6.3 ms (equivalent SRV of 0.17 cm s^{-1}). The performance of the Pd–Ag alloy (3:1 and 10 μm thick) sheet is comparable to that of Pd, and the alloy restricts the phase change of Pd in the hydrogen environment that creates pin holes [159]. Hamer et al. show the lifetime improvement with the poisoning of Pd 4.5 ms post-corona charging using a pure Pd shield [158]. The effectiveness of SHP is associated with the application of corona to the Si–SiO$_2$ interface. With only SHP, the measured lifetime of a p-type Si is ~0.5 ms, almost half of the lifetime obtained by corona charging (~1 ms), and the same improves to 2.2 ms with both SHP and corona charging [62]. Table 7 lists the reported works on the SHP with the obtained maximum effective lifetime.

Though SHP is an effective passivation method, hydrogen introduction to n-type FZ Si at ~350 °C without any dielectric layer generates hydrogen-related defects (active recombination complexes) that degrade the effective lifetime [162,166]. On the other hand, SHP does not produce defects in the case of p-type FZ Si without an additional dielectric layer [162]. Different charge states of atomic hydrogen contribute to different behavior in n-type and p-type Si. Atomic hydrogen in n-type Si exists in H^0 and H^- states, whereas in p-type Si, it exists only in the H^+ state [167,168]. So, the existence of the multiple charge states of atomic hydrogen in n-type Si increases the probability of defects.

4. Chemical passivation

The effect of heat treatment on the lifetime of the wafer can be minimized using the chemical method at room temperature. The generalized band bending concept explains the mechanism of chemical passivation, as shown in Fig. 9. The oxidation and reduction potential (E_{ox} and E_{red}) of the electrolyte must be higher than the conduction (E_{cs}) and valence band (E_{vs}) of the Si substrate for effective passivation.
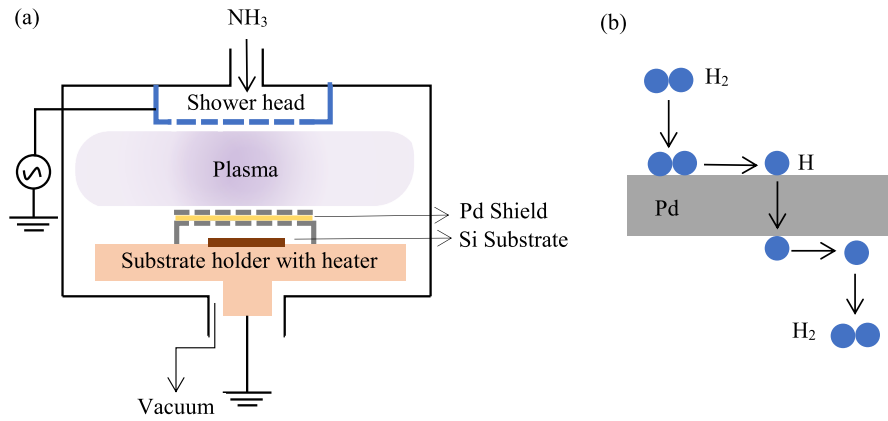
Fig. 8. (a) Set up for the metal shield in the plasma chamber, (b) possible mechanism of H diffusion on Pd.

Table 7

Summary SHP passivation (Substrate resistivity of 1 Ω cm and SiO$_2$ dielectric layer).

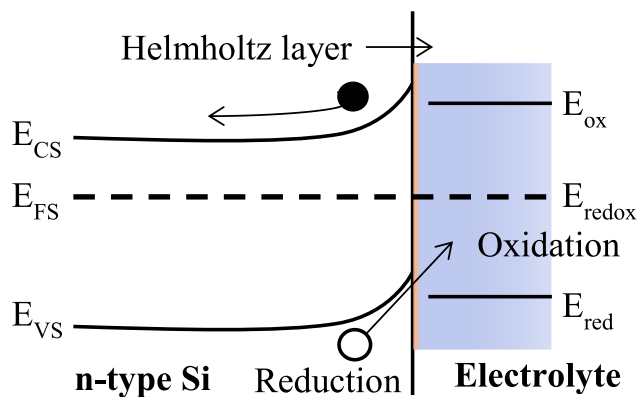| Substrate doping type	SiO$_2$ thickness (nm)	SHP details	Maximum τ_{eff} (ms)	Ref.
n-type	100	Pd (10 μm)	0.012	[159]
		Sulfur poisoned Pd	1.05	
		Pd with corona charging	4.5	
		Sulfur poisoned Pd with corona charging	6.3	
p-type	10	Only corona charging	1	[62]
		Sulfur poisoned Pd	0.5	
		Sulfur poisoned Pd with corona charging	2.2	

Fig. 9. The generalized band-bending concept for chemical passivation.

Electrons from the valence band of the Si cross the semiconductor-electrolyte interface to take part in the oxidation of the electrolyte, leading to the upward bending of the Si band structure. Accumulating the reciprocal charge at the interface on the electrolyte side creates the Helmholtz layer that restricts the electrons from jumping to the conduction band (during photon absorption) [43]. Chemical passivation uses electrolytes such as hydrofluoric acid (HF), (halogen + alcohol), and (benzyl + alcohol) solutions [169]. The lifetime measurement of chemical passivation is conducted by immersing the cleaned wafer in an electrolyte solution in an airtight plastic transparent container.

HF passivation is popular among all the solution-based chemical methods, where HF etches the unwanted oxide formation from the surface to passivate the dangling bonds with Si–F bonds. Due to the high electronegativity of fluorine atoms, surface Si atoms are etched out as SiF$_4$ forming a nonpolar [170] hydrogen-terminated (Si–H) surface [171–173] and leading to surface passivation (Fig. 10(a)). Michalak et al. reported the passivation of Si {111} surface with NH$_4$F-HF solution (buffered HF) with a higher τ_{eff} than HF passivation [174]. Grant et al. show the passivation with HF (2%): HCl (2%) is ~5 times more effective than HF (50%), and the former improves passivation with a longer duration of treatment, whereas the latter worsens [175]. The same study also reports that bis(trifluoromethane) sulfonimide (TFSI)-pentane superacid treatment after HF (2%) + HCl (2%) immersion enhances the passivation by ~ 6 times (Table 8).

Halogen-based passivation requires different solvent environments, such as ethanol, methanol, and benzene [66] and can be explained by either the halogen termination or ethoxylation of the surface. Firstly, iodine or bromine atoms replace hydrogen from the hydrogenated c-Si surface to form Si–I or Si–Br bonds due to the electro-negativity of halogen atoms [191]. Secondly, the electrons from the surface of the substrate dissociate the I$_2$ to form I$^-$, which converts the H-terminated surface (produced by HF dip) to ethoxy-termination (Fig. 10(b)) [190]. Iodine acts as an oxidant by acquiring an electron (I$^-$) from the Si–H surface, forming [Si–H]$^+$ ions. The ethoxy nucleophile combines with the Si atom via a coordinate bond, and protons released from the alcohol and Si surface neutralize the iodine atoms. According to Batra et al., iodine + ethanol (I + E) results in better passivation than bromine + ethanol (Br + E) [189]. Iodine produces higher saturation of dangling bonds than bromine as the dissociation of iodine (in alcohol) is higher due to lower bond strength (151 kJ mol^{-1} as compared to 193 kJ mol^{-1} of Br–Br).

Quinhydrone (QHY) is the equimolar charge transfer complex of *p*-benzoquinone (BQ) and hydroquinone (HQ). Two phenomena illustrate the mechanism of benzyl passivation. Firstly, BQ gains proton from methanol to form semiquinone (SQ), and due to the change in the ratio of HQ and BQ, HQ acts as a reducing agent for BQ. Thus, SQ is created both by the oxidation of HQ and the reduction of BQ. As a result, methanol retains the H$^+$ ions, and SQ formation and passivation occur in the methanol environment [195].

Secondly, BQ grabs the H atom directly from the Si–H surface to become semiquinone and reacts with the Si cation to form the Si-SQ surface. On the other hand, SQ gets H$^+$ from methanol and forms methoxide (CH$_3$O$^-$), combining with Si cation to become methoxy-Si [177]. Excessive SQ species lead to competition for adsorption between the active SQ and CH$_3$O$^-$ species on the Si surface (Fig. 10(c)); however, the SQ species are grafted to the Si–H surface to maximize the coverage before the CH$_3$O$^-$ species. Then the CH$_3$O$^-$ replaces the
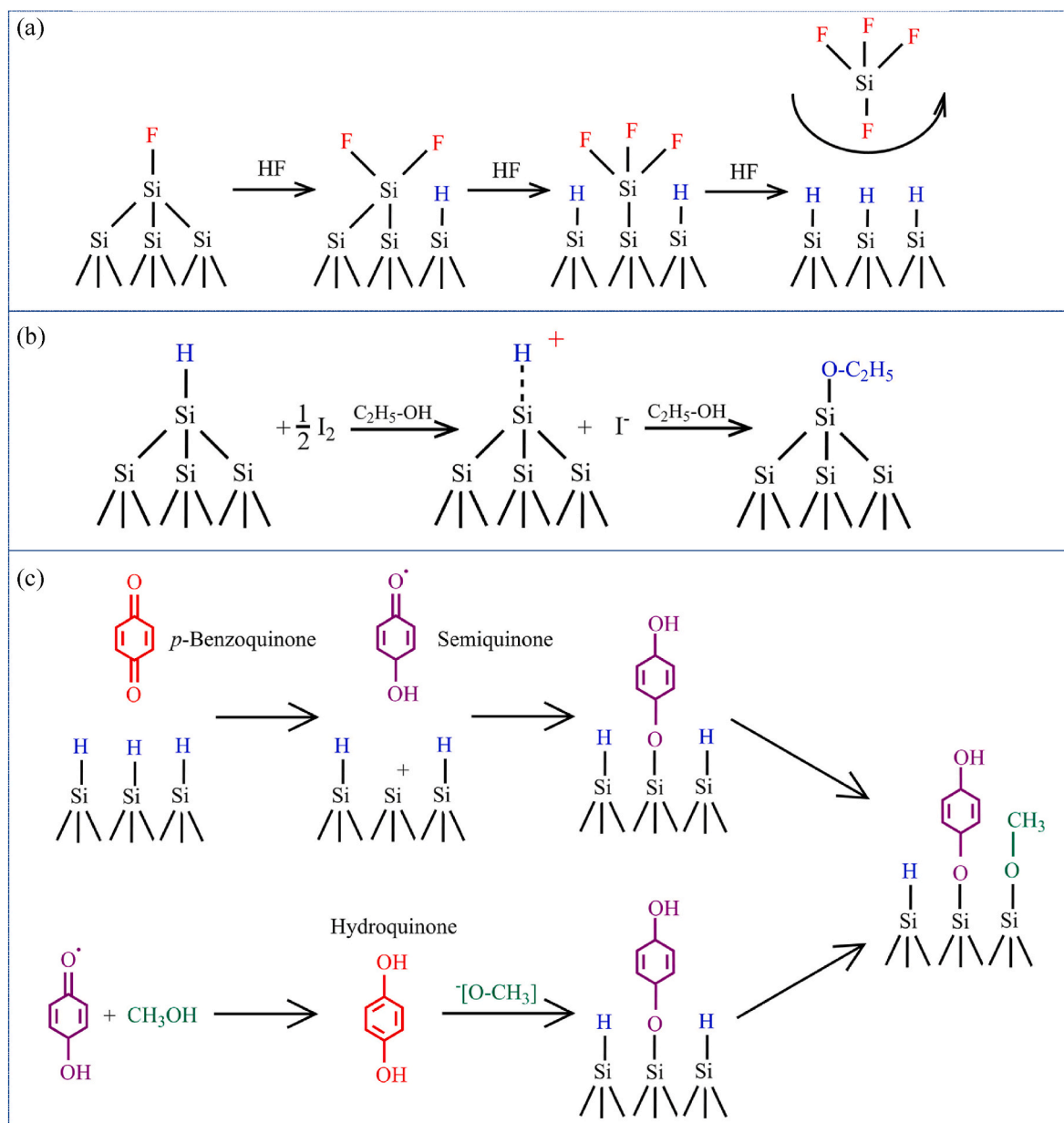
Fig. 10. Mechanism of passivations in (a) HF [176], (b) halogen + alcohol solution, and (c) benzyl + alcohol solution [177].

grafted SQ on the Si surface due to lower adsorption energies and may cause in weakening of molecular field-effect passivation [194]. Effective passivation is due to the synergistic effect of Si dangling bond saturation and the field-effect of the interface dipoles. The latter is due to the more electronegative oxygen atoms bonded to surface Si atoms [196].

For the (benzyl + methanol) or (iodine + alcohol)-based passivation, the Si wafer is cleaned by either piranha solution or RCA cleaning procedure to remove organic residues from the surface of the wafer [10]. The surface must be H-terminated by dipping the wafer into the HF solution. Finally, the H-terminated Si surface is immersed in passivating chemical solutions such as I + M or QHY + M. Before every stage, deionized (DI) water wash and N_2 gun drying may be followed [169, 196].

The degree of passivation depends on the electrolyte (chemical and solvent), substrate properties such as doping type, and resistivity. Fig. 11 (a), (b), and (c) represent the variation of τ_{eff} of passivated substrates of different resistivities for acid, halogen, and benzyl passivation. τ_{eff} is higher for the substrates with higher resistivity, and the trend is similar

for all the chemicals. The increase in resistivity restricts the flow of the charge carrier to the surface, reducing the SRV. The concept is valid for p-type and n-type substrates with similar variation trends irrespective of the chemical used for passivation. Fig. 11(d) shows the comparison of passivation of the p-type and n-type substrate (of the same resistivity) with certain chemicals at a constant concentration. τ_{eff} of the n-type substrate is higher than that of the p-type substrate for all the passivating chemicals.

Lifetime is measured when the substrate is submerged in the chemical, and removal of the substrate from the chemical reduces the stability of the passivation [198]. Fig. 12(a) shows the maximum τ_{eff} measured after removing the substrates from QHY + M (0.01 M) solution at different time intervals. For both p-type (2 Ω cm) and n-type (100 Ω cm) substrates, with increased environmental exposure, τ_{eff} decreases due to oxidation and removal of the passivating benzyl group [198]. The QHY + alcohol passivation is more stable than (I + E) or (I + M) passivation [197,201] and the mechanism of the passivation degradation is depicted in Fig. 12(b).

Table 8

List of the solution-based chemicals used for passivation of the c-Si.

Type	Chemical (concentration)	Si doping type, Resistivity (Ω.cm)	Wafer thickness (μm)	Maximum τ_{eff} (ms)	SRV (cm.s^{-1})	Ref.
Acid	HF (5%)	n, 100	475	0.125	184	[65]
	HF (20%)	n, 1	400	2	2.7	[178]
		n, 5	700	10	2.8	
		p, 1000	500	50	0.7	
		p, 1	400	0.2	10	[179]
	HF (40%)	p, 0.8	300	0.8	4.8	[178]
	HF (48%)	p[c], 35	525	2.9	2.8[b]	[180]
		p, 2	300	1.9	1.9[b]	
		n, 4000-6000	500	2.2	11	[174]
		p, 22	2700	2.5	1	[181]
		p, 150	250	40	0.25	[182]
	HF (50%)	n, 5	110	0.18	194[b]	[175]
	HF (50%) + SA[a]			1.5	23.3[b]	
	HF (2%) + HCl (2%)			0.85	41.2[b]	
	HF (2%) + HCl (2%) + SA[a]			5.5	6.4[b]	
Halogen	I + E (0.03 M)	n[c], 6.7	1190	1.82	5.5	[183]
	I + E (0.08 M)	n, 1-10	500	0.9	28	[184]
		n, 1.7–13	180	0.97	5.2	[185]
		n, 100	430	2.72	7.9	[186]
		p, 100	279	1.7	8,2	
		p, 200	220	6	1.8	[187]
		p, 5	650	0.177	192	[188]
		p, 5	650	0.78	–	[189]
	I + E (0.1 M)	n, 8-12	350	10	–	[190]
		n (111), 30	350	20	–	
		n, 5	640	8	–	[191]
		n, 3- 5	1490	46	6.2	
		n (111), 60	360	17	–	
		p, 12.8	–	0.25	–	[192]
	I + M (0.08 M)	p, 5	650	0.171	194	[188]
	I + M (0.09 M)	p, 22	2700	3.25	0.75	[181]
		n, 100	475	0.65	35	[169]
		n, 3	280	0.23	60	
		n, 1	170	0.09	89	
		n, 100	475	0.89	25	[65]
	Br + E (0.06 M)	p, 5	650	0.121	282	[188]
	Br + E (0.08 M)			0.78	–	[189]
	Br + M (0.06 M)			0.15	227	[188]
	Br + M (0.08 M)	n, 2.6–3.4	200	–	20	[181]
Benzyl	BQ + M (0.1 M)	n, 25	500	3.25	8[b]	[193]
		p	525	1.9	14[b]	
		n	280	4.5	1.6	[194]
	BQ + M (10 mM)	n, 100	450	3.39	6.64[b]	[195]
	HQ + M (10 mM)	n, 100	450	0.09	250[b]	[195]
	QHY + M (1 mM)	n, 0.1	300	0.47	31.9[b]	[196]
	QHY + M (10 mM)	n, 100	450	2.81	8.0[b]	[195]
		n[c], 1	170	0.67	12.6	[169]
		n[c], 3	280	1.36	10.2	
		p, 5	650	0.7	–	[197]
		p, 150	380	4.5	–	
		n, 100	460	3.3	–	[198]
		p, 2	280	1.1	–	
		n, 100	460	3.3	7	[199]
		n, 3	280	1.36	–	
		n, 1	170	0.67	–	
		n, 100	475	2.2	10.4	[65]
	QHY + M (70 mM)	p, 200	220	8.5	–	[187]
		n, 2	–	0.18	–	[177]
	QHY + E (10 mM)	p, 5	650	0.6	–	[197]
		p, 150	400	4.1	4.6	[200]

[a] Bis(trifluoromethane)sulfonimide (TFSI)-pentane superacid treatment.

[b] Calculated considering infinite bulk lifetime.

[c] Czochralski (CZ) wafer and rest are Float-zone (FZ) wafers.

5. Laser passivation

One of the approaches to minimize the solar cell fabrication cost is the use of upgraded metallurgical grade (UMG) wafers instead of semiconductor grade. However, the cell efficiency decreases due to the higher bulk defects such as B–O complex formation and metallic impurities at the grain boundaries. Advanced hydrogen passivation reduces the recombination due to the bulk defects using laser technology, making the UMG wafers suitable for efficient solar cell production. Though a laser is used for the dielectric layer ablation and grooving of the semiconductor surface for the contact formation, passivation of the bulk defects is possible with a laser source by changing the charge states of atomic hydrogen with the laser parameters [202]. The hydrogen charge states play an essential role in the passivation of defects, such as the neutralization of dopant atoms (B^- by H^+ and P^+ by H^-), the passivation of impurities (Fe^+ by H^-), and the permanent deactivation
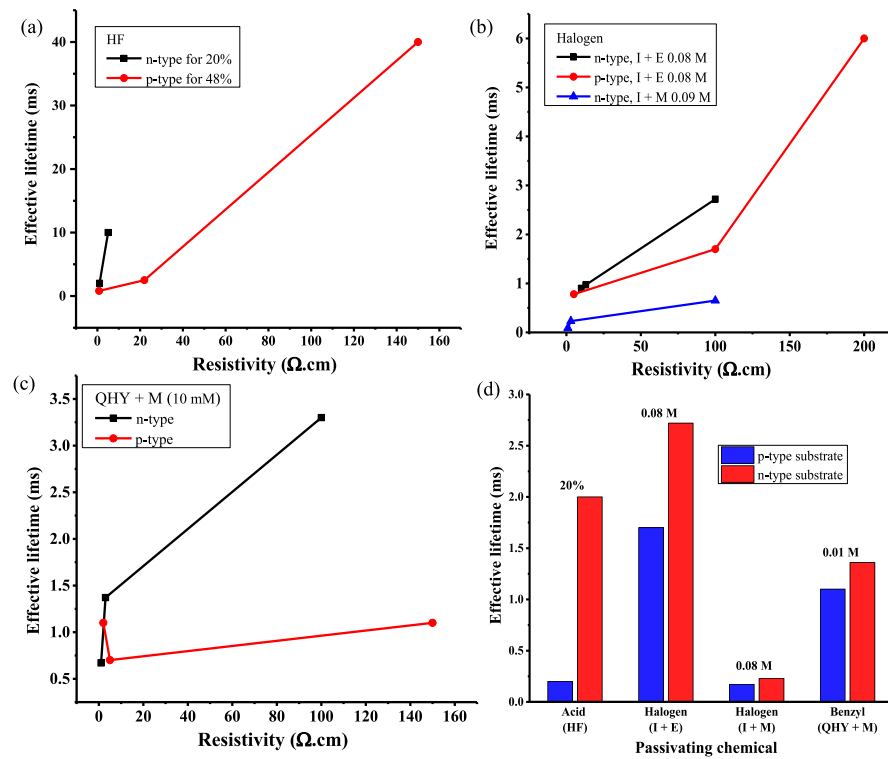
Fig. 11. Dependency of τ_{eff} on the resistivity of the substrate passivated by (a) HF acid, (b) halogen- (I + E) & (I + M), (c) benzyl- (QHY + M) at constant concentrations; (d) Comparison of passivation of p-type and n-type substrate with different chemicals.
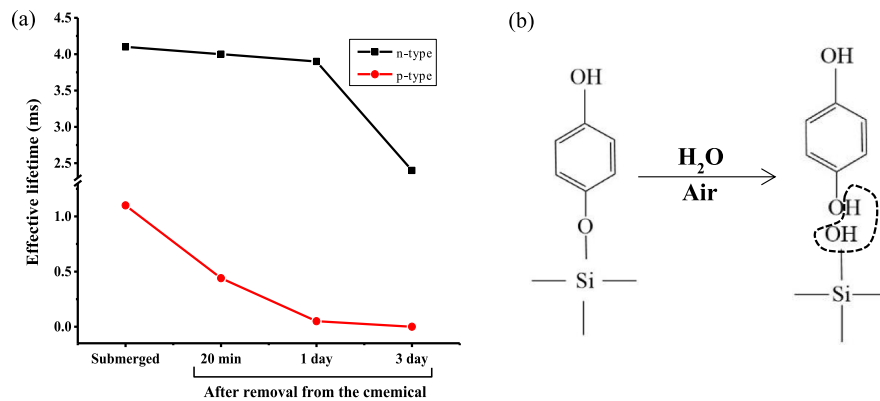

Fig. 12. (a) Variation of effective lifetime after removing the sample from the QHY + M (0.01 M) solution, representing the temporary passivation; (b) mechanism of degradation of passivation by QHY + M [198].
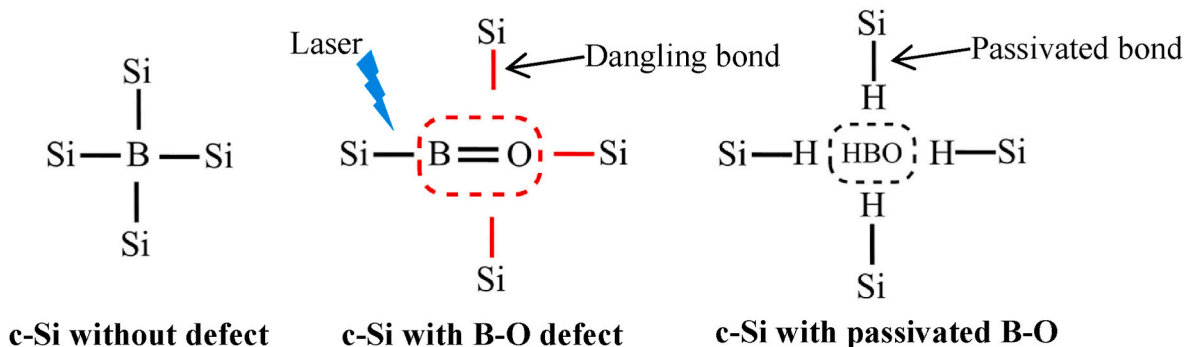

Fig. 13. Mechanism of laser hydrogen passivation of B–O defect.

of B–O complex (by H^+ or H^0).

The position of the Fermi level to the hydrogen donor and acceptor levels dominates the relative hydrogen concentration of a given charge state [203,204]. A hydrogen donor level is at 0.16 eV below the conduction band for the donor level, and a hydrogen acceptor level is at 0.07 eV below the middle band gap [204]. In p-type Si, the ionized boron atoms (B^-) attract the H^+ due to the Coulombic attraction at moderate temperatures [205]. Similarly, ionized phosphorus atoms (P^+) retract the diffused H^- in n-type Si [206]. In contrast, H^0 is unaffected by fixed charges, such as ionized dopant atoms and charged defects within the Si.

The bulk defects create dangling bonds that act as the recombination centers leading to a reduction in V_{oc}. Trapped oxygen in the B-doped substrate creates a B–O complex with Si leaving three Si-dangling bonds aside, as depicted in Fig. 13 (a possible passivation mechanism). Although the bond dissociation energy of Si–B (= 289 kJ mol^{-1}) is weaker as compared to the Si–H (= 298.5 kJ mol^{-1}), only the atomic hydrogen introduction to the defect site does not neutralize all the dangling bonds [172,207]. Laser illumination breaks the Si–B bond and alters the charge state of the atomic hydrogen to combine with the Si-dangling bonds and the B–O complex to form either borane (HBO) or hydroxyl boron (HOBO). During subsequent high-temperature processes (the wafer goes through until the solar cell fabrication), the probability of breaking the Si–H bond is higher than that of the B–H bond (= 330 kJ mol^{-1}), leading to dehydrogenation and recreation of the recombination center [208]. Hence, trapping enough atomic hydrogen is extremely important during hydrogenation.

The temperature and the illumination control the minority charge carrier, and the injection of the minority carrier controls the charge state of the hydrogen, enhancing the passivation [209,210]. Laser, being the source of heat and illumination and having comprehensive control over various parameters, is used for hydrogen passivation of a localized area of Si. Wang et al. showed that the laser hydrogenation temperature affects the passivation more than the illumination intensity (laser power) [211]. After a short period of 1 min, the influence of the illumination intensity saturates, whereas the process temperature affects the hydrogenation. With an increase in temperature, the diffusivity of the atomic hydrogen improves; however, the effectiveness degrades at higher temperatures due to the loose stability of the atomic hydrogen during the cooling from elevated temperatures.

The laser wavelength selection is another crucial factor for successful laser-induced hydrogenation. According to Hamer et al., irradiation with a long-wavelength laser is appropriate for hydrogenation [212]. Longer wavelengths allow homogenous carrier production over the bulk, a reduction in low energy, and the ability to manipulate the charge state of atomic hydrogen with greater temperature control. Several aspects involved in laser-assisted hydrogen passivation are i. atomic hydrogen introduction to the bulk of the substrate, ii. diffusion of the atomic hydrogen throughout the substrate, iii. activation of the appropriate charge state of the atomic hydrogen at the recombination sites, and iv. trapping of the hydrogen in the substrate to avoid the release during subsequent processes.

High temperature shifts the Fermi level towards the middle of the band gap in p-type Si, achieving a higher ratio of minority charge states of atomic hydrogen and increasing the hydrogen release rate from the PECVD-grown SiN_x layer as the source of atomic hydrogen [213,214]. Forming gas and NH_3 are the sources of hydrogen for the thermally grown SiO_2 layer (introduced during annealing) and PECVD-grown $SinN_x$ layer. High-temperature passivation also leads to rapid dissociation of hydrogen-defect complexes, which limits the effectiveness of the process [215]. On the other hand, illumination significantly increases the relative concentrations of the minority charge states of atomic hydrogen [210]. It helps in reducing defect-reactivation during the cooling phase of high-temperature hydrogen passivation [168,209]. Si surface passivated by PECVD-SiN_x containing hydrogen shows degradation and regeneration with illumination, whereas passivation by low-pressure chemical vapor deposition (LPCVD) SiN_x without hydrogen shows only degradation and no regeneration of minority carrier [216].

Hallam et al. compared the conventional industrial hydrogen passivation with the laser passivation of p-type UMG Si and showed the improvement of a bulk lifetime from 8 to 550 μs due to the minimization of the B–O defect sites in the bulk of the substrate (Table 9) [209]. The hydrogen passivation of the B–O defect is a reversible process, i.e., the B–O defect may regenerate during the subsequent high-temperature substrate processing of cell manufacturing due to the release of the atomic hydrogen [216]. Hence a sufficient amount of atomic hydrogen should be introduced into the bulk to avoid defect-regeneration during the high-temperature processes. The introduction of laser passivation into the fabrication of the PERL solar cell based on commercial grade B-doped CZ wafer results in V_{oc} of 681 mV and a bulk lifetime of 500 μs [216]. Although laser hydrogen passivation increases the lifetime of B-doped substrates, no substantial lifetime improvement is reported in Ga-doped substrates with the SiN_x dielectric layer. Rather, Ga_2O_3 dielectric layer assists the laser passivation for Ga–Fe defects [64]; however, it lags behind the SiN_x in terms of antireflecting coating.

6. Passivation strategies in various solar cells

The efficiency improvement is the driving factor for the evolution of various solar cell architectures, from Si-based single junction Al-BSF to multi-junction TOPCon cells. For Si-based cells, both surface and bulk passivation are the critical aspects considering substrate compatibility, photon absorption [217], contact interface [218,219], and fabrication complexities [137]. Among passivation strategies, field-effect passivation and chemical passivation are the acceptable methods for surface passivation [43,72,220] however, dielectric-based field-effect passivation is the established technique and still evolving [217,221]. Though solution-based chemical passivation results in a comparative lifetime to field-effect passivation, the use of chemical passivation in solar cell fabrication is rarely reported due to its instability [43]. For investigating impurity activity in multi-crystalline Si for solar cells, liquid-based chemical passivation, especially of the halogen- or benzyl-based solutions, is useful [222–224]. SHP and laser passivation are the improvements over dielectric-based field-effect passivation for bulk defects [63, 209]. Table 1 lists the advancement of the solar cell from the passivation point of view, and the current section summarizes the passivation strategies used in various solar cells in recent years.

Table 9

List of the defects and parameters of laser passivation.

Defect passivation	Laser wavelength (nm)	Laser processing speed (m.s^{-1})	Dielectric layer	Si wafer, doping, Resistivity (Ω.cm)	Max τ_{eff} (ms)	Ref.
B–O	532	0.5	SiN_x	B-CZ, p, 2	1.4	[209]
				UMG-CZ, p, 2	0.55	
	–	–	SiN_x	p; 1.6	0.15	[211]
Ga–Fe	355	~0.33	Ga_2O_3		~3	[64]

UMG-upgraded metallurgical grade, B-CZ- Boron doped Czochralski.

6.1. PERC

PERC cell is the successor of the Al-BSF cell and is passivated on both the front and rear surface by a dielectric layer, unlike the heavily-doped rear surface of the Al-BSF cell. The efficiency of a standard Al-BSF solar cell is constrained by poor light absorption and rear-side recombination losses [225]. The direct contact of metal-Si recombination loss is caused by a significant number of metal-induced surface state densities [226]. PERC uses a dielectric layer + ARC on the front side, whereas a dielectric layer + capping layer on the rear side, as depicted in Fig. 1 (a). The dielectric layer on the front and rear side may be SiO_2, Al_2O_3, TiO_2, and HfO_2 [227] and the substrate compatibility is listed in Table 5. SiN_x is a versatile dielectric which can act as an independent dielectric layer, ARC, and rear capping layer [228–230]. The dielectric layer on the front surface is optional for SiN_x ARC; however, the dielectric layer + ARC combination surpasses in terms of performance [89,228].

Though SiO_2/SiN_x:H is the convenient passivation stacking layer for both the front and the rear surface of the PERC cell, the combination of the CZ substrate and SiO_2/SiN_x:H passivation is prone to surface-related defects caused by illumination [231]; whereas the PERC cells with Al_2O_3/SiN_x:H is safe. Similar passivation schemes are also applicable to PERL and PERT cells; however, Al_2O_3/SiN_x:H is preferred for rear surface passivation [232,233]. Though dielectric-based field-effect passivation is the only strategy used in PERC cells, laser passivation is also used for localized doping for the selective emitter and rear contacts for hydrogen defect passivation to reduce the device's dark saturation current [233,234].

6.2. IBC

The front surface of the IBC cell is fully coated with the dielectric layer + ARC, and the rear surface possesses all the contact terminals, as shown in Fig. 1 (c). As the front surface is fully utilized for photon absorption, ARC plays a significant role in efficiency improvement; however, a monolayer of ARC (SiN_x) or Al_2O_3 dielectric layer is inefficient (Table 5). The preferable passivation scheme for the front surface of the n-type substrate-based IBC cell is SiO_2/SiN_x followed by $SiO_2/Al_2O_3/SiN_x$ [235,236].

Yang et al. reported ion-implanted polysilicon as a carrier selective passivated contact on the rear side for both BSF and emitter, resulting in a well-passivated gap to minimize the shunting loss [237]. An advanced ARC was obtained by layering an ultrathin SiO_2 layer above traditional micro-textured pyramids and passivated with a-Si/SiN_x. $SiO_2/SiN_x/SiO_2$ acts as excellent passivation and ARC on the front (random pyramidal textured) and the rear surfaces to achieve 25% cell efficiency [238]. Apart from field-effect passivation, IBC cells use a thin polymer film (polystyrenesulfonate-a water-based solution spin-coated and dried) as an ARC on the front surface for surface passivation [239]. For a 150 nm thick polymer layer, a minority carrier lifetime of 2.5 ms was achieved for an n-type (280 μm thick), which showed a new technology roadmap for organic solution-based chemical passivation. Though no literature reports the hydrogen passivation via laser in IBC cells, contact passivation is possible by laser doping on n^+ and p^+ regions to optimize the contact resistance for SiO_2/a-Si:H passivation layer [240,241].

6.3. SHJ

Silicon heterojunction (SHJ) cell is one of the cell architectures with an efficiency of >25% and an open circuit voltage of >0.7 V [3]. SHJ cell uses hydrogenated intrinsic amorphous Si as the passivating layer, separating the amorphous emitter layer from crystalline substrate and indium tin oxide (ITO)/SiO_2 as the front ARC and passivating layer [242]. Parasitic absorption at the front ITO and amorphous emitter interface is the main limitation for the SHJ with both side contacts, which can be solved by the IBC structure [243]. Ding et al. reported the passivation effect of intrinsic ZnO and Al-doped ZnO, which can replace

the phosphorous-doped a-Si on an n-type c-Si substrate [244]. Solution-based ZnO and Al-doped ZnO were spin-coated and annealed to result in 17.13% and 18.46% cell efficiency, respectively, whereas the primary purpose of the layers is the electron-selective transport layer. Instead of SiO_2 and hydrogenated a-Si, as chemical passivation, spin-coated carbon nanotube passivates n-type substrate and results in 21.4% efficiency [245].

6.4. TOPCon

TOPCon cell architecture possesses two passivation schemes-surface passivation by conventional dielectric-based field-effect passivation and rear surface contact passivation by tunnel-oxide (Fig. 1 (d)). The front surface uses SiO_2 or Al_2O_3 as the dielectric layer and ITO or SiN_x as the ARC [29]. Both-sided TOPCon solar cell uses the ultrathin SiO_2 layer as the contact passivation on both surfaces [246]. The front passivation mechanism is similar to that of conventional PERC cells, i.e., the compatibility of the dielectric and ARC layer depends on the heavily-doped emitter, as listed in Table 5. However, the contact passivation through the tunnel oxide is the prime attraction for the researchers. Lu et al. studied the replacement of SiO_2 with ALD-deposited Al_2O_3 and a combination of Al_2O_3/SiO_2 [247]. Both Al_2O_3 and Al_2O_3/SiO_2 stacking fails to yield better passivation than the SiO_2 due to the increased B-diffusion and accumulation of B at Al_2O_3 or Al_2O_3/SiO_2 stacking, leading to higher recombinations through B–O defects. The effect of ITO deposition followed by annealing on the passivation quality of the p-TOPCon and n-TOPCon was reported by Tao et al. [248]. The passivation improves for annealing temperature up to 500 °C in p-TOPCon, whereas the passivation degrades in the n-TOPCon after ITO deposition and annealing indicating the compatibility of ITO with B-doped poly-Si.

7. Conclusion

Recombination is one of the major reasons that limit solar cell efficiency. As a remedy, passivation reduces recombination both at the surface and the bulk. The field-effect passivation mitigates the surface recombination by the electric field generated by the excess doping layer or by the corona charging of the dielectric layer. The electric field reduces the minority carrier concentration at the surface to minimize the possible recombination. The dielectric layer, such as (SiO_2) and (Al_2O_3) with a capping layer (SiN_x), are more effective than the dielectric layer alone as the interface quality improves. Excess-diffused deposition act as selective carrier layers for contact passivation. SHP is an extended version of field-effect passivation for further improvement of the lifetime. Pd and Sulfur poisoned Pd–Ag alloy sheets act as the shield during PECVD for hydrogen passivation of surface as well as bulk defects. Alcohol-based HF, halogens, and benzyl solutions are used for chemical passivation of the c-Si surface, facilitating the bulk lifetime measurement without actual dielectric layer deposition. Laser passivation decreases surface and bulk recombination current by passivating the defects using different charge states of the atomic hydrogen. Chemical passivation and laser passivation work on the principle of DOS reduction. Effective passivation always incorporates both the carrier concentration and DOS reduction strategies regardless of strategies. The recent development shows that standard solar cells employ dielectric-based field-effect passivation, whereas solution-based chemical passivation is unstable under atmospheric exposure and hence rarely reported for solar cell applications.

CRediT authorship contribution statement

Sakti Prasanna Muduli: Writing – original draft, Methodology, Investigation, Formal analysis, Data curation. **Paresh Kale:** Writing – review & editing, Visualization, Supervision, Project administration, Funding acquisition, Conceptualization.

Declaration of competing interest

The authors declare that they have no known competing financial interests or personal relationships that could have appeared to influence the work reported in this paper.

Data availability

No data was used for the research described in the article.

Acknowledgments

References

[1] R.K. Tarai, P. Kale, Solar PV policy framework of Indian States: overview, pitfalls, challenges, and improvements, Renewable Energy Focus 26 (2018) 46–57, https://doi.org/10.1016/j.ref.2018.07.001.

[2] K. Yoshikawa, H. Kawasaki, W. Yoshida, T. Irie, K. Konishi, K. Nakano, T. Uto, D. Adachi, M. Kanematsu, H. Uzu, K. Yamamoto, Silicon heterojunction solar cell with interdigitated back contacts for a photoconversion efficiency over 26%, Nat. Commun. 2 (2017) https://doi.org/10.1038/nenergy.2017.32.

[3] M.A. Green, E.D. Dunlop, J. Hohl-Ebinger, M. Yoshita, N. Kopidakis, K. Bothe, D. Hinken, M. Rauer, X. Hao, Solar cell efficiency tables (Version 60), Prog. Photovoltaics Res. Appl. 30 (2022) 687–701, https://doi.org/10.1002/pip.3595.

[4] SRoeCo Solar, Most Efficient Solar Panels, SRoeCo Solar Website, 2013, pp. 1–2, 2012, http://sroeco.com/solar/most-efficient-solar-panels. (Accessed 12 October 2022).

[5] T. Matsui, A. Bidiville, K. Maejima, H. Sai, T. Koida, T. Suezaki, M. Matsumoto, K. Saito, I. Yoshida, M. Kondo, High-efficiency amorphous silicon solar cells: impact of deposition rate on metastability, Appl. Phys. Lett. 106 (2015), https://doi.org/10.1063/1.4907001.

[6] M.A. Green, K. Emery, Y. Hishikawa, W. Warta, E.D. Dunlop, D.H. Levi, A.W. Y. Ho-Baillie, Solar cell efficiency tables (version 49), Prog. Photovoltaics Res. Appl. 25 (2017) 3–13, https://doi.org/10.1002/pip.2855.

[7] C. Battaglia, A. Cuevas, S. de Wolf, High-efficiency crystalline silicon solar cells: status and perspectives, Energy Environ. Sci. 9 (2016) 1552–1576, https://doi.org/10.1039/c5ee03380b.

[8] P.J. Ribeyron, Crystalline silicon solar cells: better than ever, Nat. Energy 2 (2017), https://doi.org/10.1038/nenergy.2017.67.

[9] M.K. Sahoo, P. Kale, Restructured porous silicon for solar photovoltaic: a review, Microporous Mesoporous Mater. 289 (2019), 109619, https://doi.org/10.1016/j.micromeso.2019.109619.

[10] M.K. Sahoo, P. Kale, Integration of silicon nanowires in solar cell structure for efficiency enhancement: a review, Journal of Materiomics 5 (2019) 34–48, https://doi.org/10.1016/j.jmat.2018.11.007.

[11] M.K. Sahoo, P. Kale, Transfer of vertically aligned silicon nanowires array using sacrificial porous silicon layer, Thin Solid Films (2020) 698, https://doi.org/10.1016/j.tsf.2020.137866.

[12] M.A. Green, Solar cell fill factors: general graph and empirical expressions, Solid State Electron. 24 (1981) 788–789, https://doi.org/10.1016/0038-1101(81)90062-9.

[13] V. Benda, Photovoltaics: the Basics, A Comprehensive Guide to Solar Energy Systems, 2018, pp. 151–179, https://doi.org/10.1016/b978-0-12-811479-7.00008-7.

[14] P. Kowalczewski, L.C. Andreani, Towards the efficiency limits of silicon solar cells: how thin is too thin? Sol. Energy Mater. Sol. Cell. 143 (2015) 260–268, https://doi.org/10.1016/j.solmat.2015.06.054.

[15] M.A. Green, Silicon solar cells: evolution, high-efficiency design and efficiency enhancements, Semicond. Sci. Technol. 8 (1993) 1–12, https://doi.org/10.1088/0268-1242/8/1/001.

[16] F. Cao, K. Chen, J. Zhang, X. Ye, J. Li, S. Zou, X. Su, Next-generation multi-crystalline silicon solar cells: diamond-wire sawing, nano-texture and high efficiency, Sol. Energy Mater. Sol. Cell. 141 (2015) 132–138, https://doi.org/10.1016/j.solmat.2015.05.030.

[17] Y. Zhang, J. Tao, Y. Chen, Z. Xiong, M. Zhong, Z. Feng, P. Yang, J. Chu, A large-volume manufacturing of multi-crystalline silicon solar cells with 18.8% efficiency incorporating practical advanced technologies, RSC Adv. 6 (2016) 58046–58054, https://doi.org/10.1039/c6ra05765a.

[18] A. Blakers, Development of the PERC solar cell, IEEE J. Photovoltaics 9 (2019) 629–635, https://doi.org/10.1109/JPHOTOV.2019.2899460.

[19] G. Kökbudak, E. Orhan, F. Es, E. Semiz, R. Turan, Optimization of Silicon Nitride (SiN$_X$) Anti-reflective coating (arc) and passivation layers using industrial plasma enhanced chemical vapor deposition (pecvd) for perc type solar cells, in: PVCon 2018 - International Conference on Photovoltaic Science and Technologies, 2018, https://doi.org/10.1109/PVCon.2018.8523918.

[20] B. Min, M. Müller, H. Wagner, G. Fischer, R. Brendel, P.P. Altermatt, H. Neuhaus, A roadmap toward 24% efficient PERC solar cells in industrial mass production, IEEE J. Photovoltaics 7 (2017) 1541–1550, https://doi.org/10.1109/JPHOTOV.2017.2749007.

[21] F. Li, D. Liu, Z. Wang, J. Zhai, W. Zhang, Y. Shen, J. Shi, D. Song, I. Cesar, N. Guillevin, A.R. Burgers, P. Venema, Development of large-area bifacial interdigitated-back-contact (IBC) solar cell with industrial production environment, in: 2018 IEEE 7th World Conference on Photovoltaic Energy Conversion, WCPEC 2018 - A Joint Conference of 45th IEEE PVSC, 28th PVSEC and 34th EU PVSEC, 2018, pp. 3722–3726, https://doi.org/10.1109/PVSC.2018.8547673.

[22] L.C. Andreani, A. Bozzola, P. Kowalczewski, M. Liscidini, L. Redorici, Silicon solar cells: toward the efficiency limits, Adv. Phys. X 4 (2019), 1548305, https://doi.org/10.1080/23746149.2018.1548305.

[23] J. Liu, Y. Yao, S. Xiao, X. Gu, Review of status developments of high-efficiency crystalline silicon solar cells, J. Phys. D Appl. Phys. 51 (2018), https://doi.org/10.1088/1361-6463/aaac6d.

[24] R. Peibst, M. Rienäcker, Y. Larionova, N. Folchert, F. Haase, C. Hollemann, S. Wolter, J. Krügener, P. Bayerl, J. Bayer, M. Dzinnik, R.J. Haug, R. Brendel, Towards 28 %-efficient Si single-junction solar cells with better passivating POLO junctions and photonic crystals, Sol. Energy Mater. Sol. Cell. (2022) 238, https://doi.org/10.1016/j.solmat.2021.111560.

[25] N. Anand, P. Kale, Optimization of TOPCon structured solar cell using AFORS-HET, Transactions on Electrical and Electronic Materials 22 (2021) 160–166, https://doi.org/10.1007/s42341-020-00220-0.

[26] N.C. Mandal, S. Acharya, S. Biswas, T. Panda, S. Sadhukhan, J.R. Sharma, S. Bose, G. Das, A. Kole, A. Nandi, S. Maity, P. Chaudhuri, H. Saha, S. Guha, Evolution of PERC from Al-BSF: optimization based on root cause analysis, Appl. Phys. Mater. Sci. Process 126 (2020), https://doi.org/10.1007/s00339-020-03747-4.

[27] M.A. Green, The passivated emitter and rear cell (PERC): from conception to mass production, Sol. Energy Mater. Sol. Cell. 143 (2015) 190–197, https://doi.org/10.1016/j.solmat.2015.06.055.

[28] C. Messmer, A. Fell, F. Feldmann, N. Wohrle, J. Schon, M. Hermle, Efficiency roadmap for evolutionary upgrades of PERC solar cells by TOPCon: impact of parasitic absorption, IEEE J. Photovoltaics 10 (2020) 335–342, https://doi.org/10.1109/JPHOTOV.2019.2957642.

[29] D.K. Ghosh, S. Bose, G. Das, S. Acharyya, A. Nandi, S. Mukhopadhyay, A. Sengupta, Fundamentals, present status and future perspective of TOPCon solar cells: a comprehensive review, Surface. Interfac. 30 (2022), https://doi.org/10.1016/j.surfin.2022.101917.

[30] D.D. Smith, P. Cousins, S. Westerberg, R. de Jesus-Tabajonda, G. Aniero, Y. C. Shen, Toward the practical limits of silicon solar cells, IEEE J. Photovoltaics 4 (2014) 1465–1469, https://doi.org/10.1109/JPHOTOV.2014.2350695.

[31] D. Lachenal, P. Papet, B. Legradic, R. Kramer, T. Kössler, L. Andreetta, N. Holm, W. Frammelsberger, D.L. Baetzner, B. Strahm, L.L. Senaud, J.W. Schüttauf, A. Descoeudres, G. Christmann, S. Nicolay, M. Despeisse, B. Paviet-Salomon, C. Ballif, Optimization of tunnel-junction IBC solar cells based on a series resistance model, Sol. Energy Mater. Sol. Cell. 200 (2019), 110036, https://doi.org/10.1016/j.solmat.2019.110036.

[32] P. Wang, R. Sridharan, X.R. Ng, J.W. Ho, R. Stangl, Development of TOPCon tunnel-IBC solar cells with screen-printed fire-through contacts by laser patterning, Sol. Energy Mater. Sol. Cell. 220 (2021), 110834, https://doi.org/10.1016/j.solmat.2020.110834.

[33] A. Richter, F. Werner, A. Cuevas, J. Schmidt, S.W. Glunz, Improved parameterization of Auger recombination in silicon, Energy Proc. 27 (2012) 88–94, https://doi.org/10.1016/j.egypro.2012.07.034.

[34] W. Michaelis, M.H. Pilkuhn, Radiative recombination in silicon p-n junctions, Phys. Status Solidi 36 (1969) 311–319, https://doi.org/10.1002/pssb.19690360132.

[35] A. Schenk, An improved approach to the Shockley-Read-Hall recombination in inhomogeneous fields of space-charge regions, J. Appl. Phys. 71 (1992) 3339–3349, https://doi.org/10.1063/1.350929.

[36] E. Yablonovitch, T.J. Gmitter, A contactless minority lifetime probe of heterostructures, surfaces, interfaces and bulk wafers, Solid State Electron. 35 (1992) 261–267, https://doi.org/10.1016/0038-1101(92)90230-A.

[37] E. Yablonovitch, D.L. Allara, C.C. Chang, T. Gmitter, T.B. Bright, Unusually low surface-recombination velocity on silicon and germanium surfaces, Phys. Rev. Lett. 57 (1986) 249–252, https://doi.org/10.1103/PhysRevLett.57.249.

[38] R.A. Sinton, A. Cuevas, Contactless determination of current-voltage characteristics and minority-carrier lifetimes in semiconductors from quasi-steady-state photoconductance data, Appl. Phys. Lett. 69 (1996) 2510–2512, https://doi.org/10.1063/1.117723.

[39] A. Kimmerle, J. Greulich, A. Wolf, Carrier-diffusion corrected J0-analysis of charge carrier lifetime measurements for increased consistency, Sol. Energy Mater. Sol. Cell. 142 (2015) 116–122, https://doi.org/10.1016/j.solmat.2015.06.043.

[40] undefined K. Luke, L.C. J. of A. Physics, Analysis of the interaction of a laser pulse with a silicon wafer: determination of bulk lifetime and surface recombination velocity, Aip.Scitation.Org. 61 (1987) (1987) 2282, https://doi.org/10.1063/1.337938.

[41] A.B. Sproul, Dimensionless solution of the equation describing the effect of surface recombination on carrier decay in semiconductors, J. Appl. Phys. 76 (1994) 2851–2854, https://doi.org/10.1063/1.357521.

[42] R.S. Bonilla, B. Hoex, P. Hamer, P.R. Wilshaw, Dielectric surface passivation for silicon solar cells: a review, Physica Status Solidi (A) Applications and Materials Science (2017) 214, https://doi.org/10.1002/pssa.201700293.

[43] N.E. Grant, J.D. Murphy, Temporary surface passivation for characterisation of bulk defects in silicon: a review, Phys. Status Solidi Rapid Res. Lett. 11 (2017), https://doi.org/10.1002/pssr.201700243.

[44] W. Shockley, W.T. Read, Statistics of the recombinations of holes and electrons, Phys. Rev. 87 (1952) 835–842, https://doi.org/10.1103/PhysRev.87.835.

[45] R.B.M. Girisch, R.P. Mertens, R.F. de Keersmaecker, Determination of Si-SiO$_2$ interface recombination parameters using a gate-controlled point-junction diode under illumination, IEEE Trans. Electron. Dev. 35 (1988) 203–222, https://doi.org/10.1109/16.2441.

[46] K.R. McIntosh, L.E. Black, On effective surface recombination parameters, J. Appl. Phys. 116 (2014), https://doi.org/10.1063/1.4886595.

[47] H. Mäckel, K. Varner, On the determination of the emitter saturation current density from lifetime measurements of silicon devices, Prog. Photovoltaics Res. Appl. 21 (2013) 850–866, https://doi.org/10.1002/pip.2167.

[48] R. Dumbrell, M.K. Juhl, T. Trupke, Z. Hameiri, Extracting surface saturation current density from lifetime measurements of samples with metallized surfaces, in: 2018 IEEE 7th World Conference on Photovoltaic Energy Conversion, WCPEC 2018 - A Joint Conference of 45th IEEE PVSC, 28th PVSEC and 34th EU PVSEC, 2018, pp. 3243–3247, https://doi.org/10.1109/PVSC.2018.8547720.

[49] A. Kimmerle, J. Greulich, A. Wolf, Carrier-diffusion corrected J0-analysis of charge carrier lifetime measurements for increased consistency, Sol. Energy Mater. Sol. Cell. 142 (2015) 116–122, https://doi.org/10.1016/j.solmat.2015.06.043.

[50] X. Yang, H. Xu, W. Liu, Q. Bi, L. Xu, J. Kang, M.N. Hedhili, B. Sun, X. Zhang, S. de Wolf, Atomic layer deposition of vanadium oxide as hole-selective contact for crystalline silicon solar cells, Adv Electron Mater 6 (2020), 2000467, https://doi.org/10.1002/aelm.202000467.

[51] B. Hoex, S.B.S. Heil, E. Langereis, M.C.M. van de Banden, W.M.M. Kessels, Ultralow surface recombination of c-Si substrates passivated by plasma-assisted atomic layer deposited Al2O3, Appl. Phys. Lett. 89 (2006), 042112, https://doi.org/10.1063/1.2240736.

[52] S. de Wolf, C. Ballif, M. Kondo, Kinetics of a-Si:H bulk defect and a-Si:H/c-Si interface-state reduction, Phys. Rev. B Condens. Matter 85 (2012), 113302, https://doi.org/10.1103/PhysRevB.85.113302.

[53] A. Augusto, J. Karas, P. Balaji, S.G. Bowden, R.R. King, Exploring the practical efficiency limit of silicon solar cells using thin solar-grade substrates, J Mater Chem A Mater 8 (2020) 16599–16608, https://doi.org/10.1039/d0ta04575f.

[54] M. Zhang, J. Chen, W. Xuan, X. Song, H. Xu, J. Zhang, J. Wu, H. Jin, S. Dong, J. Luo, Comparison of sputtering and atomic layer deposition based ultra-thin alumina protective layers for high temperature surface acoustic wave devices, J. Mater. Res. Technol. 15 (2021) 4714–4724, https://doi.org/10.1016/j.jmrt.2021.10.081.

[55] R.S. Bonilla, N. Jennison, D. Clayton-Warwick, K.A. Collett, L. Rands, P. R. Wilshaw, Corona charge in SiO2: kinetics and surface passivation for high efficiency silicon solar cells, Energy Proc. 92 (2016) 326–335, https://doi.org/10.1016/j.egypro.2016.07.090.

[56] R.S. Bonilla, C. Reichel, M. Hermle, P. Hamer, P.R. Wilshaw, Long term stability of c-Si surface passivation using corona charged SiO2, Appl. Surf. Sci. 412 (2017) 657–667, https://doi.org/10.1016/j.apsusc.2017.03.204.

[57] S.W. Glunz, F. Feldmann, SiO2 surface passivation layers – a key technology for silicon solar cells, Sol. Energy Mater. Sol. Cell. 185 (2018) 260–269, https://doi.org/10.1016/j.solmat.2018.04.029.

[58] B. Hoex, J. Schmidt, R. Bock, P.P. Altermatt, M.C.M. van de Sanden, W.M. M. Kessels, Excellent passivation of highly doped p -type Si surfaces by the negative-charge-dielectric Al$_2$O$_3$, Appl. Phys. Lett. 91 (2007), 112107, https://doi.org/10.1063/1.2784168.

[59] J. Benick, B. Hoex, M.C.M. van de Sanden, W.M.M. Kessels, O. Schultz, S. W. Glunz, High efficiency n-type Si solar cells on Al$_2$O$_3$-passivated boron emitters, Appl. Phys. Lett. 92 (2008), 253504, https://doi.org/10.1063/1.2945287.

[60] J.L. Cantin, H.J. von Bardeleben, Y. Ke, R.P. Devaty, W.J. Choyke, Hydrogen passivation of carbon P b like centers at the 3C- and 4H-SiCSiO$_2$ interfaces in oxidized porous SiC, Appl. Phys. Lett. 88 (2006), 092108, https://doi.org/10.1063/1.2179128.

[61] H.F.W. Dekkers, L. Carnel, G. Beaucarne, Carrier trap passivation in multicrystalline Si solar cells by hydrogen from SiN$_x$:H layers, Appl. Phys. Lett. 89 (2006), 013508, https://doi.org/10.1063/1.2219142.

[62] G. Bourret-Sicotte, P. Hamer, R.S. Bonilla, K. Collett, P.R. Wilshaw, Shielded hydrogen passivation - a novel method for introducing hydrogen into silicon, in: Energy Proc. (2017) 267–274, https://doi.org/10.1016/j.egypro.2017.09.298.

[63] S.H. Lee, M.F. Bhopal, D.W. Lee, S.H. Lee, Review of advanced hydrogen passivation for high efficient crystalline silicon solar cells, Mater. Sci. Semicond. Process. 79 (2018) 66–73, https://doi.org/10.1016/j.mssp.2018.01.019.

[64] T.G. Allen, M. Ernst, C. Samundsett, A. Cuevas, Demonstration of c-Si solar cells with gallium oxide surface passivation and laser-doped gallium p$^+$ regions, in: 2015 IEEE 42nd Photovoltaic Specialist Conference, PVSC 2015, 2015, https://doi.org/10.1109/PVSC.2015.7356405.

[65] B. Chhabra, S. Suzer, R.L. Opila, C.B. Honsberg, Electrical and chemical characterization of chemically passivated silicon surfaces, in: Conference Record of the IEEE Photovoltaic Specialists Conference, 2008, https://doi.org/10.1109/PVSC.2008.4922673.

[66] W. Cai, Z. Lin, T. Strother, L.M. Smith, R.J. Hamers, Chemical modification and patterning of iodine-terminated silicon surfaces using visible light, J. Phys. Chem. B 106 (2002) 2656–2664, https://doi.org/10.1021/jp013523h.

[67] D. Deligiannis, S. Alivizatos, A. Ingenito, D. Zhang, M. van Sebille, R.A.C.M. M. van Swaaij, M. Zeman, Wet-chemical treatment for improved surface

passivation of textured silicon heterojunction solar cells, in: Energy Proc. (2014) 197–202, https://doi.org/10.1016/j.egypro.2014.08.117.

[68] M. Mehler, A. Schmid, A. Zuschlag, M. Trempa, G. Hahn, Delay of regeneration by adding aluminum in boron-doped crystalline Si, Physica Status Solidi (A) Applications and Materials Science 218 (2021), 2100603, https://doi.org/10.1002/pssa.202100603.

[69] A. ur Rehman, M.Z. Iqbal, M.F. Bhopal, M.F. Khan, F. Hussain, J. Iqbal, M. Khan, S.H. Lee, Development and prospects of surface passivation schemes for high-efficiency c-Si solar cells, Sol. Energy 166 (2018) 90–97, https://doi.org/10.1016/j.solener.2018.03.025.

[70] X. Jia, F. Lv, P. Li, W. Wang, Life-cycle assessment of p-type multi-Si back surface field (BSF) solar module in China of 2019, Sol. Energy 196 (2020) 207–216, https://doi.org/10.1016/j.solener.2019.12.018.

[71] S. Park, H. Park, Y. Kang, H.S. Lee, D. Kim, Analysis of aluminum back surface field at different wafer specifications in crystalline silicon solar cells, Curr. Appl. Phys. 16 (2016) 1062–1068, https://doi.org/10.1016/j.cap.2016.05.016.

[72] J. Schmidt, R. Peibst, R. Brendel, Surface passivation of crystalline silicon solar cells: present and future, Sol. Energy Mater. Sol. Cell. 187 (2018) 39–54, https://doi.org/10.1016/j.solmat.2018.06.047.

[73] D.B.M. Klaassen, A unified mobility model for device simulation-I. Model equations and concentration dependence, Solid State Electron. 35 (1992) 953–959, https://doi.org/10.1016/0038-1101(92)90325-7.

[74] D.B.M. Klaassen, A unified mobility model for device simulation-II. Temperature dependence of carrier mobility and lifetime, Solid State Electron. 35 (1992) 961–967, https://doi.org/10.1016/0038-1101(92)90326-8.

[75] A. Schenk, Finite-temperature full random-phase approximation model of band gap narrowing for silicon device simulation, J. Appl. Phys. 84 (1998) 3684–3695, https://doi.org/10.1063/1.368545.

[76] F. Werner, B. Veith, D. Zielke, L. Kühnemund, C. Tegenkamp, M. Seibt, R. Brendel, J. Schmidt, Electronic and chemical properties of the c-Si/Al2O3 interface, J. Appl. Phys. 109 (2011), https://doi.org/10.1063/1.3587227.

[77] A.G. Aberle, S. Glunz, W. Warta, Impact of illumination level and oxide parameters on Shockley-Read-Hall recombination at the Si-SiO2 interface, J. Appl. Phys. 71 (1992) 4422–4431, https://doi.org/10.1063/1.350782.

[78] B. Hoex, J. Schmidt, P. Pohl, M.C.M. van de Sanden, W.M.M. Kessels, Silicon surface passivation by atomic layer deposited Al2 O 3, J. Appl. Phys. 104 (2008), 044903, https://doi.org/10.1063/1.2963707.

[79] B. Hoex, J.J.H. Gielis, M.C.M. van de Sanden, W.M.M. Kessels, On the c-Si surface passivation mechanism by the negative-charge-dielectric Al2 O 3, J. Appl. Phys. 104 (2008), 113703, https://doi.org/10.1063/1.3021091.

[80] F.J. Ma, G.G. Samudra, M. Peters, A.G. Aberle, F. Werner, J. Schmidt, B. Hoex, Advanced modeling of the effective minority carrier lifetime of passivated crystalline silicon wafers, J. Appl. Phys. 112 (2012), https://doi.org/10.1063/1.4749572.

[81] G. Dingemans, N.M. Terlinden, D. Pierreux, H.B. Profijt, M.C.M. van de Sanden, W.M.M. Kessels, Influence of the oxidant on the chemical and field-effect passivation of Si by ALD Al2 O3, Electrochem. Solid State Lett. 14 (2011), https://doi.org/10.1149/1.3501970/META.

[82] S.C. Vitkavage, E.A. Irene, H.Z. Massoud, An investigation of Si-SiO$_2$ interface charges in thermally oxidized (100), (110), (111), and (511) silicon, J. Appl. Phys. 68 (1990) 5262–5272, https://doi.org/10.1063/1.347042.

[83] S. Dauwe, J. Schmidt, A. Metz, R. Hezel, Fixed charge density in silicon nitride films on crystalline silicon surfaces under illumination, in: Conference Record of the IEEE Photovoltaic Specialists Conference, 2002, pp. 162–165, https://doi.org/10.1109/PVSC.2002.1190481.

[84] D. Suh, D.Y. Choi, K.J. Weber, Al2O3/TiO2 stack layers for effective surface passivation of crystalline silicon, J. Appl. Phys. 114 (2013), 154107, https://doi.org/10.1063/1.4825258.

[85] L. Pereira, P. Barquinha, E. Fortunato, R. Martins, Low temperature processed hafnium oxide: structural and electrical properties, Mater. Sci. Semicond. Process. 9 (2006) 1125–1132, https://doi.org/10.1016/j.mssp.2006.10.031.

[86] K.R. McIntosh, L.P. Johnson, Recombination at textured silicon surfaces passivated with silicon dioxide, in: J. Appl. Phys. (2009), https://doi.org/10.1063/1.3153979.

[87] B. Stegemann, J. Kegel, M. Mews, E. Conrad, L. Korte, U. Stürzebecher, H. Angermann, Passivation of textured silicon wafers: influence of pyramid size distribution, a-Si:H deposition temperature, and post-treatment, in: Energy Proc. (2013) 881–889, https://doi.org/10.1016/j.egypro.2013.07.360.

[88] Y. Qiu, L. Wang, H. Hao, W. Shi, M. Lu, A synergetic effect of surface texture and field-effect passivations on improving Si solar cell performance, Physica E Low Dimens Syst Nanostruct 71 (2015) 96–100, https://doi.org/10.1016/j.physe.2015.03.025.

[89] H. Huang, J. Lv, Y. Bao, R. Xuan, S. Sun, S. Sneck, S. Li, C. Modanese, H. Savin, A. Wang, J. Zhao, 20.8% industrial PERC solar cell: ALD Al$_2$O$_3$ rear surface passivation, efficiency loss mechanisms analysis and roadmap to 24%, Sol. Energy Mater. Sol. Cell. 161 (2017) 14–30, https://doi.org/10.1016/j.solmat.2016.11.018.

[90] D.Y. Lee, H.H. Lee, J. Yong Ahn, H. Jung Park, J.H. Kim, H.J. Kwon, J.W. Jeong, A new back surface passivation stack for thin crystalline silicon solar cells with screen-printed back contacts, in: Sol. Energy Mater. Sol. Cell. (2011) 26–29, https://doi.org/10.1016/j.solmat.2010.05.004.

[91] C.T. Nguyen, K. Ohdaira, H. Matsumura, Control of solution wettability on fine-textured crystalline silicon surface to obtain high-quality passivation for solar cells, Appl. Phys. Lett. 114 (2019), https://doi.org/10.1063/1.5085434.

[92] S. Gatz, T. Dullweber, V. Mertens, F. Einsele, R. Brendel, Firing stability of SiN$_y$/ SiN$_x$ stacks for the surface passivation of crystalline silicon solar cells, Sol. Energy

Mater. Sol. Cell. 96 (2012) 180–185, https://doi.org/10.1016/j.solmat.2011.09.051.

[93] K.M. Gad, D. Vossing, A. Richter, B. Rayner, L.M. Reindl, S.E. Mohney, M. Kasemann, Ultrathin titanium dioxide nanolayers by atomic layer deposition for surface passivation of crystalline silicon, IEEE J. Photovoltaics 6 (2016) 649–653, https://doi.org/10.1109/JPHOTOV.2016.2545404.

[94] J. Huang, M. Lee, A. Lucero, L. Cheng, J. Kim, Area-selective ALD of TiO$_2$ nanolines with electron-beam lithography, J. Phys. Chem. C 118 (2014) 23306–23312, https://doi.org/10.1021/jp5037662.

[95] S.W. Glunz, D. Biro, S. Rein, W. Warta, Field-effect passivation of the SiO2-Si interface, J. Appl. Phys. 86 (1999) 683–691, https://doi.org/10.1063/1.370784.

[96] T. Mueller, S. Schwertheim, M. Scherff, W.R. Fahrner, High quality passivation for heterojunction solar cells by hydrogenated amorphous silicon suboxide films, Appl. Phys. Lett. 92 (2008), https://doi.org/10.1063/1.2837192.

[97] M.J. Kerr, A. Cuevas, Very low bulk and surface recombination in oxidized silicon wafers, Semicond. Sci. Technol. 17 (2002) 35–38, https://doi.org/10.1088/0268-1242/17/1/306.

[98] M.L. Reed, Models of Si-SiO2 interface reactions, Semicond. Sci. Technol. 4 (1989) 980–985, https://doi.org/10.1088/0268-1242/4/12/003.

[99] G. Dingemans, F. Einsele, W. Beyer, M.C.M. van de Sanden, W.M.M. Kessels, Influence of annealing and Al 2O 3 properties on the hydrogen-induced passivation of the Si/SiO2 interface, J. Appl. Phys. 111 (2012), https://doi.org/10.1063/1.4709729.

[100] R.O. Lussow, The influence of thermal SiO[sub 2] surface constitution on the adherence of photoresists, J. Electrochem. Soc. 115 (1968) 660, https://doi.org/10.1149/1.2411384.

[101] K.A. Collett, R.S. Bonilla, P. Hamer, G. Bourret-Sicotte, R. Lobo, T. Kho, P. R. Wilshaw, An enhanced alneal process to produce SRV < 1 cm/s in 1 Ω cm n-type Si, Sol. Energy Mater. Sol. Cell. 173 (2017) 50–58, https://doi.org/10.1016/j.solmat.2017.06.022.

[102] T.S. Orlova, A.v. Ankudinov, A.M. Mavlyutov, N.N. Resnina, Effect of grain boundaries on the electron work function of ultrafine grained aluminum, Rev. Adv. Mater. Sci. 57 (2018) 110–115, https://doi.org/10.1515/rams-2018-0053.

[103] S.H. Choi, Z. Shaolin, W. Yang, Layer-number-dependent work function of MoS$_2$ nanoflakes, J. Kor. Phys. Soc. 64 (2014) 1550–1555, https://doi.org/10.3938/jkps.64.1550.

[104] T. Sahoo, P. Kale, Work function-based metal–oxide–semiconductor hydrogen sensor and its functionality: a review, Adv. Mater. Interfac. 8 (2021) 2100649, https://doi.org/10.1002/admi.202100649.

[105] A. Cuevas, P.A. Basore, G. Giroult-Matlakowski, C. Dubois, Surface recombination velocity of highly doped n-type silicon, J. Appl. Phys. 80 (1996) 3370–3375, https://doi.org/10.1063/1.363250.

[106] R.R. King, R.A. Sinton, R.M. Swanson, Studies of diffused phosphorus emitters: saturation current, surface recombination velocity, and quantum efficiency, IEEE Trans. Electron. Dev. 37 (1990) 365–371, https://doi.org/10.1109/16.46368.

[107] J. Schmidt, A.G. Aberle, Carrier recombination at silicon-silicon nitride interfaces fabricated by plasma-enhanced chemical vapor deposition, J. Appl. Phys. 85 (1999) 3626–3633, https://doi.org/10.1063/1.369725.

[108] T. Lauinger, J. Schmidt, A.G. Aberle, R. Hezel, Record low surface recombination velocities on 1 cm p-silicon using remote plasma silicon nitride passivation, Appl. Phys. Lett. 68 (1996) 1232–1234, https://doi.org/10.1063/1.115936.

[109] S.v. Ghaisas, O.S. Shinde, R.O. Dusane, N.G. Dhere, Low temperature surface passivation of silicon solar cells, in: 2017 IEEE 44th Photovoltaic Specialist Conference, PVSC 2017, 2017, pp. 2170–2171, https://doi.org/10.1109/PVSC.2017.8366678.

[110] R. Hezel, K. Jaeger, Low-temperature surface passivation of silicon for solar cells, J. Electrochem. Soc. 136 (1989) 518–523, https://doi.org/10.1149/1.2096673.

[111] R. Hezel, Silicon nitride for the improvement of silicon inversion layer solar cells, Solid State Electron. 24 (1981) 863–868, https://doi.org/10.1016/0038-1101(81)90103-9.

[112] R.S. Bonilla, I. Al-Dhahir, M. Yu, P. Hamer, P.P. Altermatt, Charge fluctuations at the Si–SiO2 interface and its effect on surface recombination in solar cells, Sol. Energy Mater. Sol. Cell. 215 (2020), 110649, https://doi.org/10.1016/j.solmat.2020.110649.

[113] J. Schmidt, F. Werner, B. Veith, D. Zielke, S. Steingrube, P.P. Altermatt, S. Gatz, T. Dullweber, R. Brendel, Advances in the surface passivation of silicon solar cells, Energy Proc. 15 (2012) 30–39, https://doi.org/10.1016/j.egypro.2012.02.004.

[114] G. Dingemans, W.M.M. Kessels, Status and prospects of Al2O3-based surface passivation schemes for silicon solar cells, J. Vac. Sci. Technol.: Vacuum, Surfaces, and Films 30 (2012), 040802, https://doi.org/10.1116/1.4728205.

[115] G. Dingemans, N.M. Terlinden, D. Pierreux, H.B. Profijt, M.C.M. van de Sanden, W.M.M. Kessels, Influence of the oxidant on the chemical and field-effect passivation of Si by ALD Al2 O 3, Electrochem. Solid State Lett. 14 (2011) H1, https://doi.org/10.1149/1.3501970/XML.

[116] A. Stesmans, V.v. Afanas'Ev, Si dangling-bond-type defects at the interface of (100)Si with ultrathin layers of SiO$_x$, Al$_2$O$_3$, and ZrO$_2$, Appl. Phys. Lett. 80 (2002) 1957–1959, https://doi.org/10.1063/1.1448169.

[117] G. Dingemans, W. Beyer, M.C.M. van de Sanden, W.M.M. Kessels, Hydrogen induced passivation of Si interfaces by Al$_2$O$_3$ films and SiO$_2$/Al$_2$O$_3$ stacks, Appl. Phys. Lett. 97 (2010), 152106, https://doi.org/10.1063/1.3497014.

[118] A.C. Bronneberg, C. Höhn, R. van de Krol, Probing the interfacial chemistry of ultrathin ALD-grown TiO$_2$ films: an in-line XPS study, J. Phys. Chem. C 121 (2017) 5531–5538, https://doi.org/10.1021/acs.jpcc.6b09468.

[119] T. Mochizuki, K. Gotoh, A. Ohta, S. Ogura, Y. Kurokawa, S. Miyazaki, K. Fukutani, N. Usami, Activation mechanism of TiOx passivating layer on crystalline Si, APEX 11 (2018), 102301, https://doi.org/10.7567/APEX.11.102301.

[120] S. Miyagawa, K. Gotoh, S. Ogura, M. Wilde, Y. Kurokawa, K. Fukutani, N. Usami, Effect of hydrogen plasma treatment on the passivation performance of TiO$_x$ on crystalline silicon prepared by atomic layer deposition, J. Vac. Sci. Technol. 38 (2020), 022410, https://doi.org/10.1116/1.5134720.

[121] S. Bhatia, I.M. Khorakiwala, P.R. Nair, A. Antony, Room temperature H$_2$ plasma treatment for enhanced passivation of silicon/TiO2 interface, Appl. Phys. Lett. 113 (2018), https://doi.org/10.1063/1.5035459.

[122] X.Y. Zhang, C.H. Hsu, Y.S. Cho, S.Y. Lien, W.Z. Zhu, S.Y. Chen, W. Huang, L. G. Xie, L.D. Chen, X.Y. Zou, S.X. Huang, Simulation and fabrication of HfO$_2$ thin films passivating si from a numerical computer and remote plasma ALD, Appl. Sci. 7 (2017) 1244, https://doi.org/10.3390/app7121244.

[123] J. Kim, S. Lee, S. Chowdhury, J. Yi, A brief review of passivation materials and process for high efficiency PERC solar cell, Transactions on Electrical and Electronic Materials 23 (2022) 1–5, https://doi.org/10.1007/s42341-021-00366-5.

[124] S. Yamaguchi, K. Nakamura, T. Semba, K. Ohdaira, Y. Marumoto, Y. Ohshita, A. Masuda, Effects of SiNx refractive index and SiO$_2$ thickness on polarization-type potential-induced degradation in front-emitter n-type crystalline-silicon photovoltaic cell modules, Energy Sci. Eng. 10 (2022) 2268–2275, https://doi.org/10.1002/ese3.1135.

[125] J. Schmidt, M. Kerr, A. Cuevas, Surface passivation of silicon solar cells using plasma-enhanced chemical-vapour-deposited SiN films and thin thermal SiO$_2$/plasma SiN stacks, Semicond. Sci. Technol. 16 (2001) 164–170, https://doi.org/10.1088/0268-1242/16/3/308.

[126] B. Hoex, J. Schmidt, R. Bock, P.P. Altermatt, M.C.M. van de Sanden, W.M. M. Kessels, Excellent passivation of highly doped p -type Si surfaces by the negative-charge-dielectric Al$_2$O$_3$, Appl. Phys. Lett. 91 (2007), https://doi.org/10.1063/1.2784168.

[127] A. Richter, J. Benick, M. Hermle, Boron emitter passivation with Al2O 3 and Al 2 O3/SiNx stacks using ALD Al2O 3, IEEE J. Photovoltaics 3 (2013) 236–245, https://doi.org/10.1109/JPHOTOV.2012.2226145.

[128] N. Wehmeier, B. Lim, A. Nowack, J. Schmidt, T. Dullweber, R. Brendel, 21.0%-Efficient Co-diffused screen printed N-type silicon solar cell with rear-side boron emitter, Phys. Status Solidi Rapid Res. Lett. 10 (2016) 148–152, https://doi.org/10.1002/pssr.201510393.

[129] N.M. Nursam, K.J. Weber, H. Jin, Y. Ren, P. Smith, Investigation of interface properties in oxide passivated boron diffused silicon, Curr. Appl. Phys. 10 (2010), https://doi.org/10.1016/j.cap.2010.02.053.

[130] J. Zhao, J. Schmidt, A. Wang, G. Zhang, B.S. Richards, M.A. Green, Performance instability in N-type pert silicon solar cells, in: Proceedings of the 3rd World Conference on Photovoltaic Energy Conversion. A, 2003, pp. 923–926. https://ieeexplore.ieee.org/abstract/document/1305433/. (Accessed 16 May 2022).

[131] J. Benick, B. Hoex, O. Schultz, S.W. Glunz, Surface passivation of boron diffused emitters for high efficiency solar cells, in: Conference Record of the IEEE Photovoltaic Specialists Conference, 2008, https://doi.org/10.1109/PVSC.2008.4922637.

[132] P.P. Altermatt, H. Plagwitz, R. Bock, J. Schmidt, R. Brendel, M.J. Kerr, A. Cuevas, The surface recombination velocity at boron-doped emitters: comparison between various passivation techniques, in: 21st European Photovoltaic Energy Conference, 2006, pp. 4–7. Dresden, Germany.

[133] S. Dauwe, L. Mittelstädt, A. Metz, R. Hezel, Experimental evidence of parasitic shunting in silicon nitride rear surface passivated solar cells, Prog. Photovoltaics Res. Appl. 10 (2002) 271–278, https://doi.org/10.1002/pip.420.

[134] J. Schmidt, A. Merkle, R. Brendel, B. Hoex, M.C.M. van de Sanden, W.M. M. Kessels, Surface passivation of high-efficiency silicon solar cells by atomic-layer-deposited Al$_2$O$_3$, Prog. Photovoltaics Res. Appl. 16 (2008) 461–466, https://doi.org/10.1002/pip.823.

[135] B. Hoex, S.B.S. Heil, E. Langereis, M.C.M. van de Banden, W.M.M. Kessels, Ultralow surface recombination of c-Si substrates passivated by plasma-assisted atomic layer deposited Al$_2$O$_3$, Appl. Phys. Lett. 89 (2006), https://doi.org/10.1063/1.2240736.

[136] J. Schmidt, B. Veith, R. Brendel, Effective surface passivation of crystalline silicon using ultrathin Al$_2$O$_3$ films and Al2O3/SiN x stacks, Phys. Status Solidi Rapid Res. Lett. 3 (2009) 287–289, https://doi.org/10.1002/pssr.200903272.

[137] B. Veith, F. Werner, D. Zielke, R. Brendel, J. Schmidt, Comparison of the thermal stability of single Al2O3 layers and Al2O3/SiNx stacks for the surface passivation of silicon, in: Energy Proc. (2011) 307–312, https://doi.org/10.1016/j.egypro.2011.06.141.

[138] H. Liu, Y. Wang, L. Dong, H. Wang, Z. Zhang, Improved Al2O3/SiNx and SiO2/SiNx stack passivation layer structure PERC sc-silicon solar cells on mass production line, Int. J. Energy Res. 45 (2021) 5806–5814, https://doi.org/10.1002/er.6201.

[139] H. Hannebauer, T. Dullweber, U. Baumann, T. Falcon, R. Brendel, 21.2%-efficient fineline-printed PERC solar cell with 5 busbar front grid, Phys. Status Solidi Rapid Res. Lett. 8 (2014) 675–679, https://doi.org/10.1002/pssr.201409190.

[140] R. Brendel, R. Peibst, Contact selectivity and efficiency in crystalline silicon photovoltaics, IEEE J. Photovoltaics 6 (2016) 1413–1420, https://doi.org/10.1109/JPHOTOV.2016.2598267.

[141] R. Brendel, T. Dullweber, R. Peibst, C. Kranz, A. Merkle, D. Walter, Breakdown of the efficiency gap to 29% based on experimental input data and modeling, Prog. Photovoltaics Res. Appl. 24 (2016) 1475–1486, https://doi.org/10.1002/pip.2696.

[142] Y. Wan, C. Samundsett, J. Bullock, M. Hettick, T. Allen, D. Yan, J. Peng, Y. Wu, J. Cui, A. Javey, A. Cuevas, Conductive and stable magnesium oxide electron-selective contacts for efficient silicon solar cells, Adv. Energy Mater. 7 (2017), https://doi.org/10.1002/aenm.201601863.

[143] R. Brendel, R. Peibst, Contact selectivity and efficiency in crystalline silicon photovoltaics, IEEE J. Photovoltaics 6 (2016) 1413–1420, https://doi.org/10.1109/JPHOTOV.2016.2598267.

[144] X. Yang, K. Weber, Z. Hameiri, S. de Wolf, Industrially feasible, dopant-free, carrier-selective contacts for high-efficiency silicon solar cells, Prog. Photovolt. Res. Appl. 25 (2017) 896–904, https://doi.org/10.1002/pip.2901.

[145] D. Yan, A. Cuevas, J. Bullock, Y. Wan, C. Samundsett, Phosphorus-diffused polysilicon contacts for solar cells, Sol. Energy Mater. Sol. Cell. 142 (2015) 75–82, https://doi.org/10.1016/j.solmat.2015.06.001.

[146] M. Rienacker, M. Bossmeyer, A. Merkle, U. Romer, F. Haase, J. Krugener, R. Brendel, R. Peibst, Notice of Removal: junction resistivity of carrier selective polysilicon on oxide junctions and its impact on the solar cell performance, in: 2017 IEEE 44th Photovoltaic Specialist Conference, PVSC 2017, 2017, pp. 1–7, https://doi.org/10.1109/PVSC.2017.8366491.

[147] D. Yan, A. Cuevas, Y. Wan, J. Bullock, Passivating contacts for silicon solar cells based on boron-diffused recrystallized amorphous silicon and thin dielectric interlayers, Sol. Energy Mater. Sol. Cell. 152 (2016) 73–79, https://doi.org/10.1016/j.solmat.2016.03.033.

[148] S.Y. Herasimenka, W.J. Dauksher, S.G. Bowden, 750 mV open circuit voltage measured on 50 μm thick silicon heterojunction solar cell, Appl. Phys. Lett. 103 (2013), https://doi.org/10.1063/1.4817723.

[149] J. Bullock, A. Cuevas, T. Allen, C. Battaglia, Molybdenum oxide MoOx: a versatile hole contact for silicon solar cells, Appl. Phys. Lett. 105 (2014), https://doi.org/10.1063/1.4903467.

[150] R. Brendel, T. Dullweber, R. Peibst, C. Kranz, A. Merkle, D. Walter, Breakdown of the efficiency gap to 29% based on experimental input data and modeling, Prog. Photovolt. Res. Appl. 24 (2016) 1475–1486, https://doi.org/10.1002/pip.2696.

[151] G. Nogay, J. Stuckelberger, P. Wyss, E. Rucavado, C. Allebé, T. Koida, M. Morales-Masis, M. Despeisse, F.J. Haug, P. Löper, C. Ballif, Interplay of annealing temperature and doping in hole selective rear contacts based on silicon-rich silicon-carbide thin films, Sol. Energy Mater. Sol. Cell. 173 (2017) 18–24, https://doi.org/10.1016/j.solmat.2017.06.039.

[152] J. Geissbühler, J. Werner, S. Martin De Nicolas, L. Barraud, A. Hessler-Wyser, M. Despeisse, S. Nicolay, A. Tomasi, B. Niesen, S. de Wolf, C. Ballif, 22.5% efficient silicon heterojunction solar cell with molybdenum oxide hole collector, Appl. Phys. Lett. 107 (2015), https://doi.org/10.1063/1.4928747.

[153] F. Duerinckx, J. Szlufcik, Defect passivation of industrial multicrystalline solar cells based on PECVD silicon nitride, Sol. Energy Mater. Sol. Cell. 72 (2002) 231–246, https://doi.org/10.1016/S0927-0248(01)00170-2.

[154] C.G. van de Walle, J. Neugebauer, Hydrogen in semiconductors, Annu. Rev. Mater. Res. 36 (2006) 179–198, https://doi.org/10.1146/annurev.matsci.36.010705.155428.

[155] M. Sheoran, D.S. Kim, A. Rohatgi, H.F.W. Dekkers, G. Beaucarne, M. Young, S. Asher, Hydrogen diffusion in silicon from plasma-enhanced chemical vapor deposited silicon nitride film at high temperature, Appl. Phys. Lett. 92 (2008), 172107, https://doi.org/10.1063/1.2917467.

[156] G. Dingemans, W.M.M. Kessels, Status and prospects of Al2O3 -based surface passivation schemes for silicon solar cells, J. Vac. Sci. Technol.: Vacuum, Surfaces, and Films 30 (2012), 040802, https://doi.org/10.1116/1.4728205.

[157] F. Feldmann, M. Bivour, C. Reichel, M. Hermle, S.W. Glunz, Passivated rear contacts for high-efficiency n-type Si solar cells providing high interface passivation quality and excellent transport characteristics, Sol. Energy Mater. Sol. Cell. 120 (2014) 270–274, https://doi.org/10.1016/j.solmat.2013.09.017.

[158] P. Hamer, G. Bourret-Sicotte, G. Martins, A. Wenham, R.S. Bonilla, P. Wilshaw, A novel source of atomic hydrogen for passivation of defects in silicon, Phys. Status Solidi Rapid Res. Lett. 11 (2017), https://doi.org/10.1002/pssr.201600448.

[159] G. Bourret-Sicotte, P. Hamer, R.S. Bonilla, K. Collett, A. Ciesla, J. Colwell, P. R. Wilshaw, Shielded hydrogen passivation − A potential in-line passivation process, Physica Status Solidi (A) Applications and Materials Science (2017) 214, https://doi.org/10.1002/pssa.201700383.

[160] M.A. Pick, K. Sonnenberg, A model for atomic hydrogen-metal interactions - application to recycling, recombination and permeation, J. Nucl. Mater. 131 (1985) 208–220, https://doi.org/10.1016/0022-3115(85)90459-3.

[161] G. Bourret-Sicotte, P. Hamer, R.S. Bonilla, K. Collett, P.R. Wilshaw, Shielded hydrogen passivation - a novel method for introducing hydrogen into silicon, Energy Proc. 124 (2017) 267–274, https://doi.org/10.1016/j.egypro.2017.09.298.

[162] G. Bourret-Sicotte, P.G. Hamer, D. Tweddle, R.S. Bonilla, P.R. Wilshaw, Hydrogen related defects in float zone silicon investigated using a shielded hydrogen plasma, in: 2018 IEEE 7th World Conference on Photovoltaic Energy Conversion, WCPEC 2018 - A Joint Conference of 45th IEEE PVSC, 28th PVSEC and 34th EU PVSEC, 2018, pp. 298–302, https://doi.org/10.1109/PVSC.2018.8547713.

[163] W. Lisowski, E. Nowicka, Z. Wolfram, R. Duś, Atomic hydrogen desorption from thin palladium hydride films, Appl. Surf. Sci. 31 (1988) 157–162, https://doi.org/10.1016/0169-4332(88)90029-3.

[164] Y.I. Tyurin, I.P. Chernov, Nonequilibrium release of atomic hydrogen from metals during radiation, Dokl. Akad. Nauk 367 (1999) 328–332. https://www.sciencedirect.com/science/article/pii/S0360319901001537. (Accessed 15 April 2022).

[165] M. Bacal, A.M. Bruneteau, A.I. Livshits, V.N. Alimov, M.E. Notkin, Hydrogen superpermeable membrane operation under plasma conditions, Fusion Eng. Des. 65 (2003) 423–427, https://doi.org/10.1016/S0920-3796(03)00012-7.

[166] N.M.P. Johnson, F.A. Ponce, R.A. Street, R.J. Nemanich, Defects in single-crystal silicon induced by hydrogenation, Phys. Rev. B 35 (1987) 4166–4169, https://doi.org/10.1103/PhysRevB.35.4166.

[167] N.M. Johnson, C. Herring, Charge states of hydrogen in p-type and n-type silicon, Mater. Sci. Forum 38–41 (1991) 961–966. https://doi.org/10.4028/www.scientific.net/msf.38-41.961.

[168] P. Hamer, B. Hallam, S. Wenham, M. Abbott, Manipulation of hydrogen charge states for passivation of P-type wafers in photovoltaics, IEEE J. Photovoltaics 4 (2014) 1252–1260, https://doi.org/10.1109/JPHOTOV.2014.2339494.

[169] B. Chhabra, C. Weiland, R.L. Opila, C.B. Honsberg, Surface characterization of quinhydrone-methanol and iodine-methanol passivated silicon substrates using X-ray photoelectron spectroscopy, Physica Status Solidi (A) Applications and Materials Science 208 (2011) 86–90, https://doi.org/10.1002/pssa.201026101.

[170] W. Peng, S.M. Rupich, N. Shafiq, Y.N. Gartstein, A.v. Malko, Y.J. Chabal, Silicon surface modification and characterization for emergent photovoltaic applications based on energy transfer, Chem. Rev. 115 (2015) 12764–12796, https://doi.org/10.1021/acs.chemrev.5b00085.

[171] N.E. Grant, Light enhanced hydrofluoric acid passivation: a sensitive technique for detecting bulk silicon defects, JoVE (Journal of Visualized Experiments). 2016 (2016), e53614, https://doi.org/10.3791/53614.

[172] R. Chandra Muduli, P. Kale, Chemically modified surface of silicon nanostructures to enhance hydrogen uptake capabilities, Int. J. Hydrogen Energy (2022), https://doi.org/10.1016/j.ijhydene.2022.06.030.

[173] S.P. Muduli, P. Kale, Free-standing nanowire layer-transfer parametric optimisation of multi-response process by Grey Taguchi design, Mater. Sci. Technol. (2022) 1–9, https://doi.org/10.1080/02670836.2022.2129203.

[174] D.J. Michalak, F. Gstrein, N.S. Lewis, The role of band bending in affecting the surface recombination velocities for Si(111) in contact with aqueous acidic electrolytes, J. Phys. Chem. C 112 (2008) 5911–5921, https://doi.org/10.1021/jp075354s.

[175] N.E. Grant, A.I. Pointon, R. Jefferies, D. Hiller, Y. Han, R. Beanland, M. Walker, J. D. Murphy, Atomic level termination for passivation and functionalisation of silicon surfaces, Nanoscale 12 (2020) 17332–17341, https://doi.org/10.1039/d0nr03860a.

[176] I.P. Kalinkin, S.A. Kukushkin, A.v. Osipov, Effect of chemical treatment of a silicon surface on the quality and structure of silicon-carbide epitaxial films synthesized by atom substitution, Semiconductors 52 (2018) 802–808, https://doi.org/10.1134/S1063782618060118.

[177] R. Har-Lavan, R. Schreiber, O. Yaffe, D. Cahen, Molecular field effect passivation: quinhydrone/methanol treatment of n-Si(100), J. Appl. Phys. 113 (2013), https://doi.org/10.1063/1.4793497.

[178] N.E. Grant, K.R. McIntosh, J.T. Tan, Evaluation of the bulk lifetime of silicon wafers by immersion in hydrofluoric acid and illumination, ECS Journal of Solid State Science and Technology 1 (2012) P55–P61, https://doi.org/10.1149/2.003202jss.

[179] K.L. Luke, L. Cheng, A chemical/microwave technique for the measurement of bulk minority carrier lifetime in silicon wafers, J. Electrochem. Soc. 135 (1988) 957–961, https://doi.org/10.1149/1.2095849.

[180] R.A. Razera, A. Moehlecke, I. Zanesco, Minority carrier lifetime estimation by photoconductance decay for silicon wafers immersed in HF, IEEE J. Photovoltaics 7 (2017) 1004–1008, https://doi.org/10.1109/JPHOTOV.2017.2706420.

[181] H. M'saad, J. Michel, J.J. Lappe, L.C. Kimerling, Electronic passivation of silicon surfaces by halogens, J. Electron. Mater. 23 (1994) 487–491, https://doi.org/10.1007/BF02671234.

[182] E. Yablonovitch, D.L. Allara, C.C. Chang, T. Gmitter, T.B. Bright, Unusually low surface-recombination velocity on silicon and germanium surfaces, Phys. Rev. Lett. 57 (1986) 249–252, https://doi.org/10.1103/PhysRevLett.57.249.

[183] T. Maekawa, Y. Shima, Effect of steady bias light on carrier lifetime in silicon wafers with chemically passivated surfaces, Jpn. J. Appl. Phys. 2 (1996) 35, https://doi.org/10.1143/JJAP.35.L133.

[184] M. Ju, Y.J. Lee, K. Lee, C. Han, Y. Jo, J. Yi, Effectiveness of iodine termination for ultrahigh efficiency solar cells as a means of chemical surface passivation, Jpn. J. Appl. Phys. 51 (2012), https://doi.org/10.1143/JJAP.51.09MA03.

[185] J. Chen, L. Zhao, H. Diao, B. Yan, S. Zhou, Y. Tang, W. Wang, Surface passivation of silicon wafers by iodine-ethanol (I-E) for minority carrier lifetime measurements, Adv. Mater. Res. 652–654 (2013) 901–905. https://doi.org/10.4028/www.scientific.net/AMR.652-654.901.

[186] A.W. Stephens, M.A. Green, Effectiveness of 0.08 molar iodine in ethanol solution as a means of chemical surface passivation for photoconductance decay measurements, Sol. Energy Mater. Sol. Cell. 45 (1997) 255–265, https://doi.org/10.1016/S0927-0248(96)00061-X.

[187] K.L. Pollock, J. Junge, G. Hahn, Detailed investigation of surface passivation methods for lifetime measurements on P-type silicon wafers, IEEE J. Photovoltaics 2 (2012) 1–6, https://doi.org/10.1109/JPHOTOV.2011.2174337.

[188] N. Batra, Vandana, P. Kumar, S.K. Srivastava, P.K. Singh, X-ray photoelectron spectroscopic study of silicon surface passivation in alcoholic iodine and bromine solutions, J. Renew. Sustain. Energy 6 (2014), https://doi.org/10.1063/1.4863087.

[189] N. Batra, Vandana, S. Kumar, M. Sharma, S.K. Srivastava, P. Sharma, P.K. Singh, A comparative study of silicon surface passivation using ethanolic iodine and bromine solutions, Sol. Energy Mater. Sol. Cell. 100 (2012) 43–47, https://doi.org/10.1016/j.solmat.2011.04.028.

[190] B. Sopori, P. Rupnowski, J. Appel, D. Guhabiswas, L.T. Anderson-Jackson, Light-induced passivation of Si by iodine ethanol solution, Mater. Res. Soc. Symp. Proc. 1123 (2009) 137–144, https://doi.org/10.1557/proc-1123-1123-p07-10.

[191] M. Al-Amin, N.E. Grant, A.I. Pointon, J.D. Murphy, Iodine–ethanol surface passivation for measurement of millisecond carrier lifetimes in silicon wafers with different crystallographic orientations, Physica Status Solidi (A) Applications and Materials Science (2019) 216, https://doi.org/10.1002/pssa.201900257.

[192] B. Sopori, P. Rupnowski, J. Appel, V. Mehta, C. Li, S. Johnston, Wafer preparation and iodine-ethanol passivation procedure for reproducible minority-carrier lifetime measurement, in: Conference Record of the IEEE Photovoltaic Specialists Conference, 2008, https://doi.org/10.1109/PVSC.2008.4922688.

[193] N.A. Kotulak, M. Chen, N. Schreiber, K. Jones, R.L. Opila, Examining the free radical bonding mechanism of benzoquinone- and hydroquinone-methanol passivation of silicon surfaces, Appl. Surf. Sci. 354 (2015) 469–474, https://doi.org/10.1016/j.apsusc.2015.02.127.

[194] M. Chen, J.H. Hack, A. Iyer, K.J. Jones, R.L. Opila, Radical-driven silicon surface passivation by benzoquinone- and hydroquinone-methanol and photoinitiators, J. Phys. Chem. C 121 (2017) 21364–21373, https://doi.org/10.1021/acs.jpcc.7b05686.

[195] J.Y. Choi, Understanding of molecular contribution of quinhydrone/methanol organic passivation for improved minority carrier lifetime on nanostructured silicon surface, Appl. Sci. (2019) 9, https://doi.org/10.3390/app9183645.

[196] Z. Zou, W. Liu, D. Wang, Z. Liu, E. Jiang, S. Wu, J. Zhu, W. Guo, J. Sheng, J. Ye, Electron-selective quinhydrone passivated back contact for high-efficiency silicon/organic heterojunction solar cells, Sol. Energy Mater. Sol. Cell. 185 (2018) 218–225, https://doi.org/10.1016/j.solmat.2018.05.041.

[197] H. Takato, I. Sakata, R. Shimokawa, Quinhydrone/Methanol treatment for the measurement of carrier lifetime in silicon substrates, Jpn. J. Appl. Phys. 2 (2002) 41, https://doi.org/10.1143/jjap.41.l870.

[198] B. Chhabra, S. Bowden, R.L. Opila, C.B. Honsberg, High effective minority carrier lifetime on silicon substrates using quinhydrone-methanol passivation, Appl. Phys. Lett. 96 (2010), https://doi.org/10.1063/1.3309595.

[199] R.L. Opila, D. Yang, N. Kotulak, L. Costello, B. Chhabra, Mechanism of electrical passivation of Si surfaces with quinhydrone, in: Conference Record of the IEEE Photovoltaic Specialists Conference, 2012, pp. 2583–2587, https://doi.org/10.1109/PVSC.2012.6318123.

[200] H. Takato, I. Sakata, R. Shimokawa, Surface passivation effect of silicon substrates due to quinhydrone/ethanol treatment, Jpn. J. Appl. Phys. 2 (2001) 40, https://doi.org/10.1143/jjap.40.l1003.

[201] H. Takato, I. Sakata, R. Shimokawa, Surface passivation of silicon substrates using quinhydrone/methanol treatment, in: Proceedings of the 3rd World Conference on Photovoltaic Energy Conversion. B, 2003, pp. 1108–1111. https://ieeexplore.ieee.org/abstract/document/1306107/. (Accessed 3 March 2022).

[202] B. Sopori, Silicon solar-cell processing for minimizing the influence of impurities and defects, J. Electron. Mater. 31 (2002) 972–980, https://doi.org/10.1007/s11664-002-0030-x.

[203] N.M. Johnson, C. Herring, C.G. van de Walle, Inverted order of acceptor and donor levels of monatomic hydrogen in silicon, Phys. Rev. Lett. 73 (1994) 130–133, https://doi.org/10.1103/PhysRevLett.73.130.

[204] C. Herring, N.M. Johnson, C.G. van de Walle, Energy levels of isolated interstitial hydrogen in silicon, Phys. Rev. B Condens. Matter 64 (2001), https://doi.org/10.1103/physrevb.64.125209, 1252091–12520927.

[205] T. Zundel, J. Weber, Trap-limited hydrogen diffusion in boron-doped silicon, Phys. Rev. B 46 (1992) 2071–2077, https://doi.org/10.1103/PhysRevB.46.2071.

[206] S.T. Pantelides, Effect of hydrogen on shallow dopants in crystalline silicon, Appl. Phys. Lett. 50 (1987) 995–997, https://doi.org/10.1063/1.97957.

[207] M. Jech, A.M. El-Sayed, S. Tyaginov, D. Waldhör, F. Bouakline, P. Saalfrank, D. Jabs, C. Jungemann, M. Waltl, T. Grasser, Quantum chemistry treatment of silicon-hydrogen bond rupture by nonequilibrium carriers in semiconductor devices, Phys Rev Appl 16 (2021), 014026, https://doi.org/10.1103/PhysRevApplied.16.014026.

[208] J.A.T. de Guzman, V.P. Markevich, J. Coutinho, N.v. Abrosimov, M.P. Halsall, A.R. Peaker, Electronic properties and structure of boron–hydrogen complexes in crystalline silicon, Solar RRL 6 (2022), 2100459, https://doi.org/10.1002/solr.202100459.

[209] B.J. Hallam, P.G. Hamer, S.R. Wenham, M.D. Abbott, A. Sugianto, A.M. Wenham, C.E. Chan, G. Xu, J. Kraiem, J. Degoulange, R. Einhaus, Advanced bulk defect passivation for silicon solar cells, IEEE J. Photovoltaics 4 (2014) 88–95, https://doi.org/10.1109/JPHOTOV.2013.2281732.

[210] L. Song, A. Wenham, S. Wang, P. Hamer, M.S. Ahmmed, B. Hallam, L. Mai, M. Abbott, E.R. Hawkes, C. Chong, S. Wenham, Laser enhanced hydrogen passivation of silicon wafers, Int. J. Photoenergy 2015 (2015), https://doi.org/10.1155/2015/193892.

[211] S. Wang, L. Mai, A. Ciesla, Z. Hameiri, D. Payne, C. Chan, B. Hallam, C.M. Chong, J. Ji, Z. Shi, S. Wenham, Advanced passivation of laser-doped and grooved solar cells, Sol. Energy Mater. Sol. Cell. 193 (2019) 403–410, https://doi.org/10.1016/j.solmat.2019.01.025.

[212] P. Hamer, S. Wang, B. Hallam, S. Wenham, C.M. Chong, A. Wenham, M. Abbott, Laser illumination for manipulation of hydrogen charge states in silicon solar cells, Phys. Status Solidi Rapid Res. Lett. 9 (2015) 111–114, https://doi.org/10.1002/pssr.201409495.

[213] F. Jiang, M. Stavola, A. Rohatgi, D. Kim, J. Holt, H. Atwater, J. Kalejs, Hydrogenation of Si from SiNx(H) films: characterization of H introduced into the Si, Appl. Phys. Lett. 83 (2003) 931–933, https://doi.org/10.1063/1.1598643.

[214] B. Sopori, Y. Zhang, N.M. Ravindra, Silicon device processing in H-ambients: H-diffusion mechanisms and influence on electronic properties, J. Electron. Mater. 30 (2001) 1616–1627, https://doi.org/10.1007/s11664-001-0181-1.

[215] K. Nakayashiki, A. Rohatgi, S. Ostapenko, I. Tarasov, Minority-carrier lifetime enhancement in edge-defined film-fed grown Si through rapid thermal processing-assisted reduction of hydrogen-defect dissociation, J. Appl. Phys. 97 (2005), https://doi.org/10.1063/1.1833577.

[216] B.J. Hallam, S.R. Wenham, P.G. Hamer, M.D. Abbott, A. Sugianto, C.E. Chan, A.M. Wenham, M.G. Eadie, G.Q. Xu, Hydrogen passivation of B-O defects in Czochralski silicon, in: Energy Proc. (2013) 561–570, https://doi.org/10.1016/j.egypro.2013.07.317.

[217] J.P. Niemelä, B. Macco, L. Barraud, A. Descoeudres, N. Badel, M. Despeisse, G. Christmann, S. Nicolay, C. Ballif, W.M.M. Kessels, M. Creatore, Rear-emitter silicon heterojunction solar cells with atomic layer deposited ZnO:Al serving as an alternative transparent conducting oxide to In2O3:Sn, Sol. Energy Mater. Sol. Cell. 200 (2019), 109953, https://doi.org/10.1016/j.solmat.2019.109953.

[218] H. Park, S. Bae, S.J. Park, J.Y. Hyun, C.H. Lee, D. Choi, D. Kang, H. Han, Y. Kang, H.S. Lee, D. Kim, Role of polysilicon in poly-Si/SiOx passivating contacts for high-efficiency silicon solar cells, RSC Adv. 9 (2019) 23261–23266, https://doi.org/10.1039/c9ra03560e.

[219] A.S. Kale, W. Nemeth, S.P. Harvey, M. Page, D.L. Young, S. Agarwal, P. Stradins, Effect of silicon oxide thickness on polysilicon based passivated contacts for high-efficiency crystalline silicon solar cells, Sol. Energy Mater. Sol. Cell. 185 (2018) 270–276, https://doi.org/10.1016/j.solmat.2018.05.011.

[220] D.W. Kim, J.W. Song, H.S. Jin, B. Yoo, J.H. Lee, T.J. Park, Sulfur-enhanced field-effect passivation using (NH4)2S surface treatment for black Si solar cells, ACS Appl. Mater. Interfaces 11 (2019) 25140–25146, https://doi.org/10.1021/acsami.9b05589.

[221] K.A. Collett, S. Du, G. Bourret-Sicotte, Z. Luo, P. Hamer, B. Hallam, R.S. Bonilla, P.R. Wilshaw, Scalable techniques for producing field-effect passivation in high-efficiency silicon solar cells, IEEE J. Photovoltaics 9 (2019) 26–33, https://doi.org/10.1109/JPHOTOV.2018.2872032.

[222] undefined K. Pollock, J. Junge, G.H.-I.J. of Photovoltaics, Detailed Investigation of Surface Passivation Methods for Lifetime Measurements on P-type Silicon Wafers, Ieeexplore.Ieee.Org., 2011. n.d. https://ieeexplore.ieee.org/abstract/document/6095308/. (Accessed 15 October 2022).

[223] M. Al-Amin, J.D. Murphy, Combining low-temperature gettering with phosphorus diffusion gettering for improved multicrystalline silicon, IEEE J. Photovoltaics 7 (2017) 1519–1527, https://doi.org/10.1109/JPHOTOV.2017.2741100.

[224] M. Al-Amin, J.D. Murphy, Increasing minority carrier lifetime in as-grown multicrystalline silicon by low temperature internal gettering, J. Appl. Phys. 119 (2016), https://doi.org/10.1063/1.4954010.

[225] S. Kashyap, J. Madan, R. Pandey, R. Sharma, Comprehensive study on the recent development of PERC solar cell, Conf. Rec. IEEE Photovolt. Spec. Conf. (2020) 2542–2546, https://doi.org/10.1109/PVSC45281.2020.9300985, 2020-June.

[226] J. Madan, Shivani, R. Pandey, R. Sharma, Device simulation of 17.3% efficient lead-free all-perovskite tandem solar cell, Sol. Energy 197 (2020) 212–221, https://doi.org/10.1016/j.solener.2020.01.006.

[227] J. Kim, M. Ju, Y. Kim, J. Yi, Chemical stoichiometry effect of hafnium oxide (HfOx) for passivation layer of PERC solar cells, Mater. Sci. Semicond. Process. 148 (2022), https://doi.org/10.1016/j.mssp.2022.106833.

[228] F. Ye, Y. Li, X. Jia, H. Guo, X. Wang, J. Ding, N. Yuan, Z. Feng, Optimization of phosphorus dopant profile of industrial p-type mono PERC solar cells, Sol. Energy Mater. Sol. Cell. 190 (2019) 30–36, https://doi.org/10.1016/j.solmat.2018.10.002.

[229] Z.G. Huang, K. Gao, X.G. Wang, C. Xu, X.M. Song, L.X. Shi, Y. Zhang, B. Hoex, W.Z. Shen, Large-area MACE Si nano-inverted-pyramids for PERC solar cell application, Sol. Energy 188 (2019) 300–304, https://doi.org/10.1016/j.solener.2019.06.015.

[230] C.H. Hsu, Y.S. Cho, W.Y. Wu, S.Y. Lien, X.Y. Zhang, W.Z. Zhu, S. Zhang, S.Y. Chen, Enhanced Si passivation and PERC solar cell efficiency by atomic layer deposited aluminum oxide with two-step post annealing, Nanoscale Res. Lett. 14 (2019), https://doi.org/10.1186/s11671-019-2969-z.

[231] C. Sen, P. Hamer, A. Soeriyadi, B. Wright, M. Wright, A. Samadi, D. Chen, B.V. Stefani, D. Zhang, J. Wu, F. Jiang, B. Hallam, M. Abbott, Impact of surface doping profile and passivation layers on surface-related degradation in silicon PERC solar cells, Sol. Energy Mater. Sol. Cell. (2022) 235, https://doi.org/10.1016/j.solmat.2021.111497.

[232] S. Sadhukhan, S. Acharyya, T. Panda, N.C. Mandal, S. Bose, A. Nandi, G. Das, et al., Evaluation of dominant loss mechanisms of PERC cells for optimization of rear passivating stacks, Surface. Interfac. 27 (2021), 101496, https://doi.org/10.1016/j.surfin.2021.101496.

[233] Z. Wang, P. Han, H. Lu, H. Qian, L. Chen, Q. Meng, N. Tang, F. Gao, Y. Jiang, J. Wu, W. Wu, H. Zhu, J. Ji, Z. Shi, A. Sugianto, L. Mai, B. Hallam, S. Wenham, Advanced PERC and PERL production cells with 20.3% record efficiency for standard commercial p-type silicon wafers, Prog. Photovoltaics Res. Appl. 20 (2012) 260–268, https://doi.org/10.1002/PIP.2178.

[234] A. Ciesla, R. Chen, S. Wang, J. Jingjia, et al., High-voltage p-type PERC solar cells with anchored plating and hydrogenation, Wiley Online Library 26 (2018) 397–401, https://doi.org/10.1002/pip.2986.

[235] Y. Chen, Y. Yang, J.K. Marmon, X. Zhang, Z. Feng, P.J. Verlinden, H. Shen, Independent Al2O3/SiNx:H and SiO2/SiNx:H passivation of p+ and n+ silicon surfaces for high-performance interdigitated back contact solar cells, IEEE J. Photovoltaics 7 (2017) 51–57, https://doi.org/10.1109/JPHOTOV.2016.2617042.

[236] M. Aleman, J. Das, T. Janssens, B. Pawlak, N. Posthuma, J. Robbelein, S. Singh, K. Baert, J. Poortmans, J. Fernandez, K. Yoshikawa, P.J. Verlinden, Development and integration of a high efficiency baseline leading to 23% IBC cells, Energy Proc. 27 (2012) 638–645, https://doi.org/10.1016/j.egypro.2012.07.122.

[237] G. Yang, P. Guo, P. Procel, G. Limodio, A. Weeber, O. Isabella, M. Zeman, High-efficiency black IBC c-Si solar cells with poly-Si as carrier-selective passivating contacts, Sol. Energy Mater. Sol. Cell. 186 (2018) 9–13, https://doi.org/10.1016/j.solmat.2018.06.019.

[238] T.C. Kho, K.C. Fong, M. Stocks, K. McIntosh, E. Franklin, S.P. Phang, W. Liang, A. Blakers, Excellent ONO passivation on phosphorus and boron diffusion

demonstrating a 25% efficient IBC solar cell, Prog. Photovoltaics Res. Appl. 28 (2020) 1034–1044, https://doi.org/10.1002/PIP.3310.

[239] J. Chen, Y. Shen, B. Chen, K. Ge, J. Guo, Z. Wang, F. Li, Y. Xu, Y. Mai, Polymer thin films for anti-reflection and passivation on the front surface of interdigitated back contact c-Si solar cell, Solar RRL 1 (2017), https://doi.org/10.1002/solr.201700079.

[240] G. Masmitja, P. Ortega, I. Martín, G. López, C. Voz, R. Alcubilla, IBC c-Si(n) solar cells based on laser doping processing for selective emitter and base contact formation, Energy Proc. 92 (2016) 956–961, https://doi.org/10.1016/j.egypro.2016.07.107.

[241] X. Yang, J. Bullock, L. Xu, Q. Bi, S. Surve, M. Ernst, K. Weber, Passivated contacts to laser doped p^+ and n^+ regions, Sol. Energy Mater. Sol. Cell. 140 (2015) 38–44, https://doi.org/10.1016/j.solmat.2015.03.026.

[242] P. Balaji, W.J. Dauksher, S.G. Bowden, A. Augusto, Improving surface passivation on very thin substrates for high efficiency silicon heterojunction solar cells, Sol. Energy Mater. Sol. Cell. (2020) 216, https://doi.org/10.1016/j.solmat.2020.110715.

[243] T.G. Allen, J. Bullock, X. Yang, A. Javey, S. de Wolf, Passivating contacts for crystalline silicon solar cells, Nat. Energy 4 (2019) 914–928, https://doi.org/10.1038/s41560-019-0463-6.

[244] J. Ding, Y. Zhou, G. Dong, M. Liu, D. Yu, F. Liu, Solution-processed ZnO as the efficient passivation and electron selective layer of silicon solar cells, Prog. Photovoltaics Res. Appl. 26 (2018) 974–980, https://doi.org/10.1002/pip.3044.

[245] J. Chen, L. Wan, H. Li, J. Yan, J. Ma, B. Sun, F. Li, B.S. Flavel, A polymer/carbon-nanotube ink as a boron-dopant/inorganic-passivation free carrier selective contact for silicon solar cells with over 21% efficiency, Adv. Funct. Mater. 30 (2020), https://doi.org/10.1002/adfm.202004476.

[246] F. Feldmann, M. Simon, M. Bivour, C. Reichel, M. Hermle, S.W. Glunz, Efficient carrier-selective p- and n-contacts for Si solar cells, Sol. Energy Mater. Sol. Cell. 131 (2014) 100–104, https://doi.org/10.1016/j.solmat.2014.05.039.

[247] L. Lu, Y. Zeng, M. Liao, J. Zheng, Y. Lin, M. Feng, Y. Zhi, H. He, W. Ding, C. Shou, G. Qin, B. Yan, J. Ye, Dopant diffusion through ultrathin AlOx and AlO_x/SiO_x tunnel layer in TOPCon structure and its impact on the passivation quality on c-Si solar cells, Sol. Energy Mater. Sol. Cell. 223 (2021), 110970, https://doi.org/10.1016/j.solmat.2021.110970.

[248] K. Tao, S. Jiang, R. Jia, Y. Zhou, P. Zhang, X. Dai, H. Sun, Z. Jin, X. Liu, The impact of indium tin oxide deposition and post annealing on the passivation property of TOPCon solar cells, Sol. Energy 176 (2018) 241–247, https://doi.org/10.1016/j.solener.2018.10.034.